

A Damping Ring for the Rapid Cycling Synchrotron

H. Lovelace III

October 2023

Electron-Ion Collider
Brookhaven National Laboratory

U.S. Department of Energy

USDOE Office of Science (SC), Nuclear Physics (NP) (SC-26)

Notice: This technical note has been authored by employees of Brookhaven Science Associates, LLC under Contract No. DE-SC0012704 with the U.S. Department of Energy. The publisher by accepting the technical note for publication acknowledges that the United States Government retains a non-exclusive, paid-up, irrevocable, world-wide license to publish or reproduce the published form of this technical note, or allow others to do so, for United States Government purposes.

DISCLAIMER

This report was prepared as an account of work sponsored by an agency of the United States Government. Neither the United States Government nor any agency thereof, nor any of their employees, nor any of their contractors, subcontractors, or their employees, makes any warranty, express or implied, or assumes any legal liability or responsibility for the accuracy, completeness, or any third party's use or the results of such use of any information, apparatus, product, or process disclosed, or represents that its use would not infringe privately owned rights. Reference herein to any specific commercial product, process, or service by trade name, trademark, manufacturer, or otherwise, does not necessarily constitute or imply its endorsement, recommendation, or favoring by the United States Government or any agency thereof or its contractors or subcontractors. The views and opinions of authors expressed herein do not necessarily state or reflect those of the United States Government or any agency thereof.

A Damping Ring for the Rapid Cycling Synchrotron

H. Lovelace III, J. Kewisch

October 19, 2023

Abstract

The Electron-Ion Collider (EIC) [1] electron accelerator chain consists of a 400 MeV electron Linear Accelerator (LINAC), the Rapid Cycling Synchrotron (RCS), and the Electron Storage Ring (ESR). The LINAC injects into the RCS, the RCS ramps to a top energy of 18 GeV and the electron beam is extracted to the ESR. To minimize the momentum spread of the 400 MeV injected beam and serve as a 28 nC electron accumulator ring, a damping ring is proposed. This ring may also serve as an intermediate energy booster for the RCS. The damping ring is not within the current baseline of the EIC project.

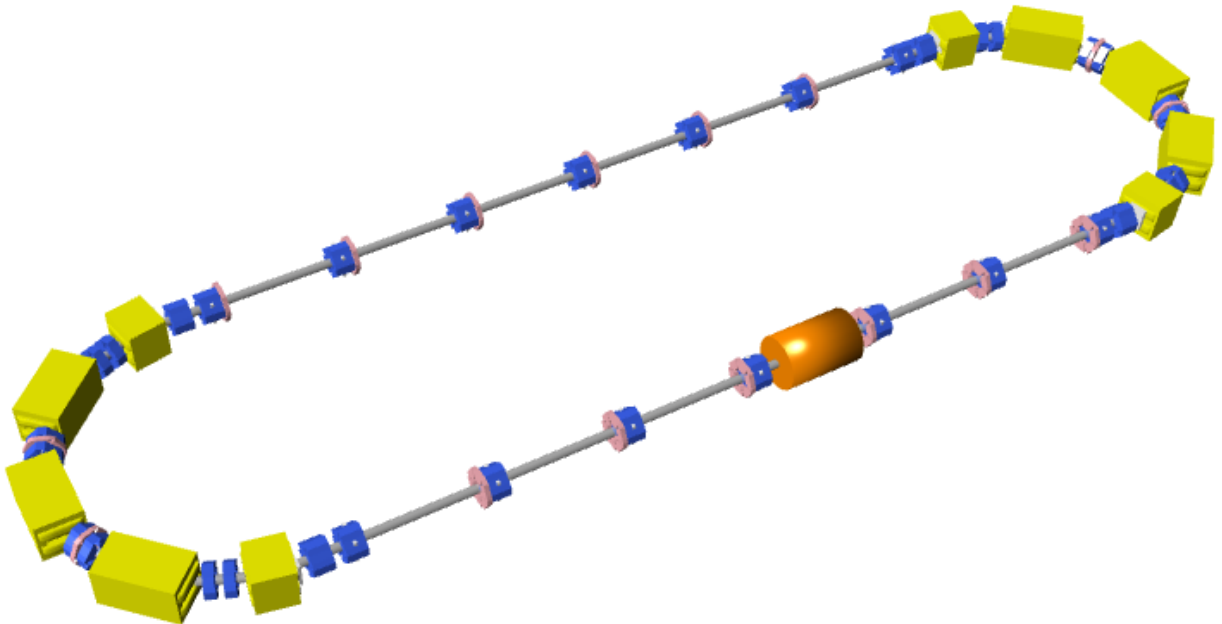


Figure 1: Floor plan of the electromagnetic elements. Yellow: dipole, blue: quadrupole, pink: sextupole, and orange: RF cavity

Contents

1	Introduction	3
1.1	A Bit of Theory	3
2	Floor Plan and Design	6
3	Optics	7
3.1	The Arc	10
3.2	The Straight Section	14
3.2.1	Longitudinal Dynamics	14
4	Dynamic Aperture	16
4.1	Optimization	17
5	Radiation Damping	18
6	Conclusion	26
7	Acknowledgments	26
A	Lattice File (damping_ring.bmad: dr-indi-arc.var)	27
B	Coordinate Transformation <i>action-angle</i>	29
C	Resonance Basis	31
D	Definition of Chirikov Criterion	32
E	W-function Derivation	33
F	Damping Ring as RCS Booster	34

1 Introduction

Traditional accumulator rings such as the Positive Intensity Accumulator (PIA) [2] [3] are designed to be compact and have an intermediate energy. The electron accumulation methods may be from individual bunch injection and bunch merging, or from injection schemes that are used for top-up injection [4]. The 400 MeV EIC LINAC delivers 7 nC per bunch. The bunch charge need for the ESR at 10 GeV and 5 GeV design energies is 28 nC. At 18 GeV the charge per bunch requirement is 11 nC. The lattice design was performed using the Bmad toolkit [5]

Due to the large energy spread, it may be necessary to damp the electron beam before injection into the RCS. At the exit end of the 400 MeV LINAC the transverse emittance is 51 nm and energy spread of 5.56×10^{-3} . Table 1 lists key damping ring (DR) lattice parameters. The RCS ramp frequency of 1 Hz requires that the damping times must be on the order of milliseconds. The 400 MeV LINAC will inject directly into the DR.

In the development of the RCS damping ring, the Chasman-Green double bend achromat [6, 7] arc lattice design was explored. It was found that the double bend achromat design of the accelerator footprint was too large. The multi-bend achromat designs were then explored [8] because of their short damping times and small accelerator footprint.

Table 1: Table of general parameters

Energy	E	400 MeV
Circumference	C	28.642 m
Horizontal Tune	ν_x	2.832
Vertical Tune	ν_y	1.562
Synchrotron Tune	ν_s	0.01175
Horizontal Natural Chromaticity	ξ_x	-11.500
Vertical Natural Chromaticity	ξ_y	6.239
Horizontal Damping Time	τ_x	13.940 ms
Vertical Damping Time	τ_y	35.985 ms
Longitudinal Damping Time	τ_z	85.963 ms
Natural Horizontal Emittance	ϵ_x	41.519 nm
Natural Bunch Length	σ_z	24.00 mm
Natural Energy Spread	δ_e	1.76×10^{-3}
Energy Loss per Turn	U_0	2.124 KeV
Revolution Frequency	ω_{rev}	10.467 MHz
Harmonic Number	h	10
RF Voltage	V	0.45 MV
RF Frequency	ω_{rf}	104.7 MHz
Momentum Compaction	α_c	7.702×10^{-2}

1.1 A Bit of Theory

At this point, it is helpful to establish a coordinate system and the Hamiltonian representation of the system. Using the Lorentz force,

$$\mathbf{F}_{e/m} = e[\mathbf{E} + \mathbf{v} \times \mathbf{B}] \quad (1)$$

, and the subsequent Langragian,

$$L = -m_0c^2\sqrt{1 - \beta^2} + e\mathbf{A} \cdot \mathbf{v} - e\phi \quad (2)$$

, where ϕ is the electric potential, \mathbf{A} is the magnetic potential, \mathbf{q}_i is the position coordinate, and \mathbf{p} is the momentum with its momenta, p_i , the Hamiltonian of a particle under electromagnetic forces can be written as:

$$\mathbf{H}(\mathbf{q}, \mathbf{p}, t) = e\phi + c\sqrt{(\mathbf{p} - e\mathbf{A})^2 + m_0^2c^2} \quad (3)$$

The equation of motion are:

$$\begin{aligned} \frac{dp_i}{dt} &= -\frac{\partial \mathbf{H}}{\partial q_i} \\ \frac{dq_i}{dt} &= \frac{\partial \mathbf{H}}{\partial p_i} \end{aligned} \quad (4)$$

We will now perform a canonical transformation to the Frenet-Serret coordinate system [9], which is shown in Fig. 2. We have that

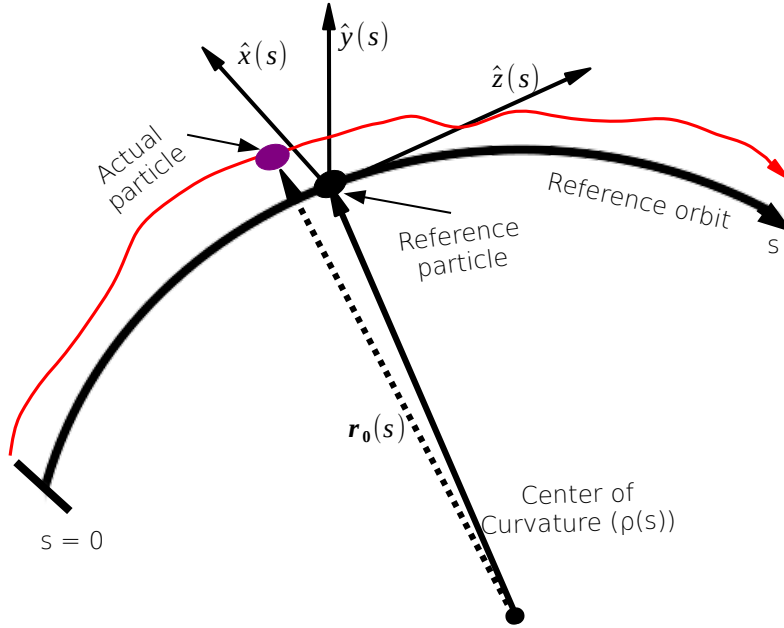


Figure 2: Frenet-Serret coordinate system where the reference particle z coordinate is zero by construction. \hat{z} is tangent, \hat{x} is normal, and \hat{y} is binormal to the curvature. \mathbf{r}_0 is the reference curve and s is the position along the reference orbit.

$$\mathbf{r}(x, y, s) = \mathbf{r}_0(s) + x\hat{x} + y\hat{y} \quad (5)$$

The triorthogonal planes of the Dreibein have the relations:

$$\begin{aligned}\frac{d\mathbf{r}_0}{ds} &= \hat{z} \\ \frac{d\hat{z}}{ds} &= \kappa\hat{x} \\ \frac{d\hat{x}}{ds} &= \tau\hat{y} - \kappa\hat{z} \\ \frac{d\hat{y}}{ds} &= -\tau\hat{x}\end{aligned}\tag{6}$$

where $\kappa = 1/\rho$ and ρ is the radius of curvature and τ is the torsion of the curve. If the reference curve is in a plane, $\tau = 0$. Using the Hamiltonian equations of motion, Equ. 4, the momentum along the direction of the reference orbit

$$p_s = \mathbf{p} \cdot \hat{z}(1 - \kappa x)\tag{7}$$

and the magnetic vector potential

$$A_s = \mathbf{A} \cdot \hat{z}(1 - \kappa x)\tag{8}$$

. Neglecting static electric field, $\phi = 0$ and the Hamiltonian is [10, 11] :

$$\mathbf{H}_s = -eA_s - (1 - \kappa x)\sqrt{\frac{H^2 - m_0^2 c^4}{c^2} - (p_x - eA_x)^2 + (p_y - eA_y)^2}\tag{9}$$

The total momentum is

$$P = \mathbf{P} \cdot \mathbf{P} = \frac{H^2 - m_0^2 c^4}{c^2} = m_0^2 c^2 (\gamma^2 - 1) = m_0^2 c^2 \beta^2 \gamma^2 = P_0 + \Delta P\tag{10}$$

With a simple transformation,

$$\bar{q} = q, \bar{s} = s, \bar{p} = p/P_0, H = H_s/P_0\tag{11}$$

where we let P_0 be the momentum of the reference particle.

$$H = -\frac{eA_s}{P_0} - (1 - \kappa x)\sqrt{\frac{P}{P_0} - (\bar{p}_x - \frac{eA_x}{P_0})^2 - (\bar{p}_y - \frac{eA_y}{P_0})^2}\tag{12}$$

The vector potential, A_s , is written as a series:

$$A_s = \sum_n A_n (x + iy)^n\tag{13}$$

The real components describe the normal field and the complex components describe the skew field. Since the magnetic field is

$$\mathbf{B} = \nabla \times \mathbf{A} \frac{eA_s}{P_0} = -\frac{B_y x^2}{2\rho^2 B_0} - \frac{1}{B_0 \rho} \sum_{n=1}^{\infty} \frac{1}{n!} \frac{\partial^{n-1} B_y}{\partial x^{n-1}} \Big|_{x=0, y=0} (x + iy)^n\tag{14}$$

The rigidity $B_0 \rho$ is a term that is produced from the total momentum and the charge of the particle species, P_0/q_{charge} . This means that B_0 is the bending field of the reference orbit at a

given curvature. We now have a description of the Hamiltonian which includes the contribution from the magnetic field written as a Taylor series

$$H = \frac{B_y|_{x=0,y=0}x^2}{2\rho^2 B_0} + \frac{1}{B_0\rho} \sum_{n=1}^{\infty} \frac{1}{n!} \frac{\partial^{n-1} B_y}{\partial x^{n-1}}|_{x=0,y=0} (x + iy)^n - (1 - \kappa x) \sqrt{\frac{P}{P_0} - (\bar{p}_x - \frac{eA_x}{P_0})^2 - (\bar{p}_y - \frac{eA_y}{P_0})^2} \quad (15)$$

The values from Tab. 1 are derived directly from the lattice using the *synchrotron radiation integrals* [12, 13].

$$\begin{aligned} I_1 &= \int_0^C G \eta ds \\ I_2 &= \int_0^C G^2 ds \\ I_3 &= \int_0^C |G^3| ds \\ I_{4_{a,b}} &= \int_0^C (G^2 + 2K_{x,y}) G \eta ds \\ I_{5_{a,b}} &= \int_0^C |G|^3 \mathcal{H}_{a,b} ds \end{aligned} \quad (16)$$

Where

$$G(s) = \mathbf{r}_0''(s) \cdot \mathbf{r}_0(s) / |\mathbf{r}_0(s)| \quad (17)$$

is the geometric strength, $K_{x,y}$ is the field gradient normalized to the rigidity, and $\eta_{a,b}$ is the mode dispersion of this uncoupled periodic system. The primes indicate the differential with respect to s . The “*dispersion invariant*”, \mathcal{H} , is

$$\mathcal{H}_{a,b} = \gamma_{a,b} \eta_{a,b}^2 + 2\alpha_{a,b} \eta'_{a,b} + \beta_{a,b} \eta_{a,b}^{\prime 2} \quad (18)$$

The α and β in Equ. 18 are the Twiss parameters [14, 15, 16].

2 Floor Plan and Design

The accelerator footprint is approximately 13×3.5 m². The circumference of the lattice is 28.64 m with straight sections composed of 3 FODO cells of length 2.75 m. The filling factor of the arc, f_f , defined by

$$L_{bend}/L_{arc} \quad (19)$$

is 0.6, where L_{bend} is the total length of the bending magnets and L_{arc} is the length of the arc. The path length through the five bend achromat arc is 5.03 m. Figure 3 illustrates the floor plan of the RCS damping ring.

The arcs of the damping ring are composed of the 5 combined function dipole magnets with 3 of the dipoles in the arc of the length 0.84 m and the other two half length, 0.42 m. The bend angle is 45°. The quadrupole lengths are .2 m and the sextupole lengths are 0.05 m. There are a

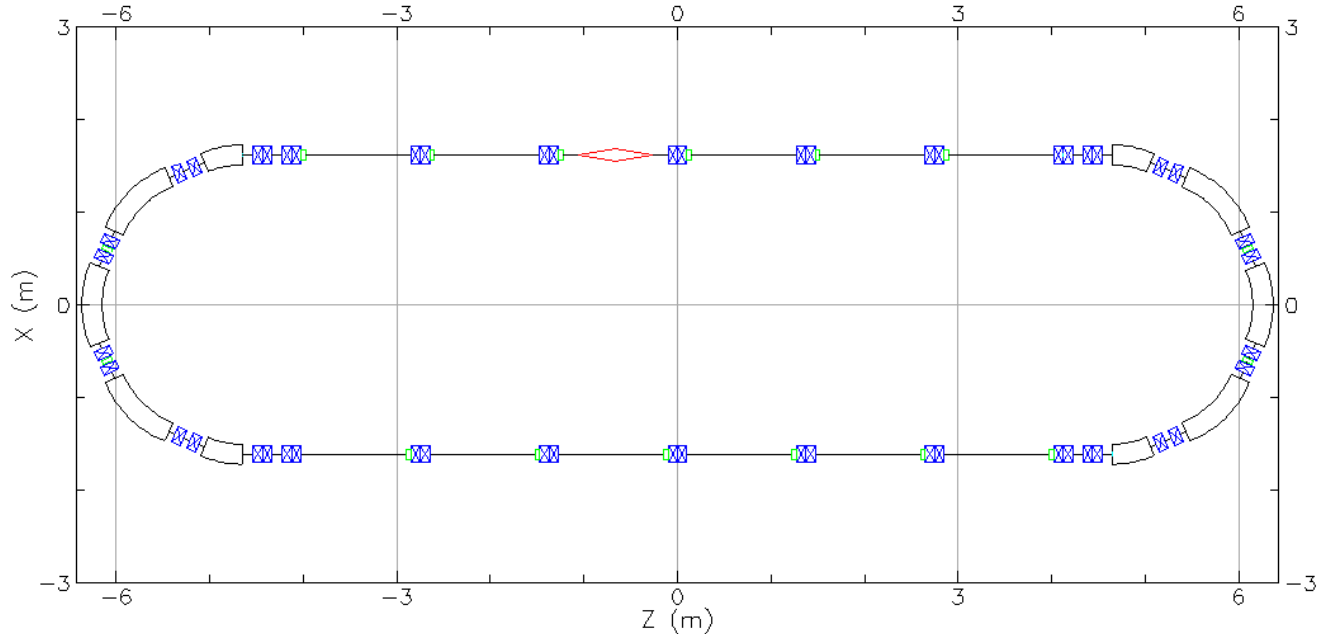


Figure 3: Floor plan of the electromagnetic elements. Black box: dipole, blue xbox: quadrupole, green xbox: sextupole, and red diamond: RF cavity. The X and Z of the coordinate system in the plot is parallel to the plane of the floor of the tunnel.

total of 10 dipoles, 26 quadrupoles and 16 sextupoles in the RCS damping ring. The dipole lengths are defined in the lattice file as:

$$L_{dipole} = R_{arc} * |\sin(\theta_{bend})| - (2 * L_{quadrupole}) \quad (20)$$

where R_{arc} is 1.75 m, θ_{bend} is $2\pi/n_{dipole}$. The number of dipoles, $n_{dipoles}$, is 8. The two half dipoles are considered one dipole in the calculations. The beam rigidity at 400 MeV is 1.33 T m. The length of the quadrupoles and sextupoles are based on the magnet design of the Compact Storage ring for Actinic Mask Inspection (COSAMI) [17]. An 80 cm RF cavity is placed in the straight section on the opposite side of the injection into the damping ring. Table 2 lists the magnets with their lengths and strengths. The RCS damping ring does not require any superconducting systems. The lattice file, in Bmad format, is located in Appendix A.

3 Optics

The lattice combines two separate beam lines, the arc and the straight section. Figure 4 plots the β -functions (both horizontal (black) and vertical (red)) and the lower plot is of the dispersion. Since there are no vertical bends, elements that excite coupling, and the lattice is ideal, the vertical dispersion (red) is zero. The tunes of the lattice $\nu_{x,y}$, are 2.832, 1.562, respectively. The fractional tunes are far enough away from the fifth order resonance horizontally and the strong half integer resonance vertically. The resonance condition can be written as:

$$pQ_x + qQ_y + rQ_s = n \quad (21)$$

where p , q , r , and n are integers. If p and q have the same sign, the resonance is known as a *sum resonance*. If the signs are different, a *difference resonance*. The highest order of resonance that is

Rapid Cycling Synchrotron Damping Ring

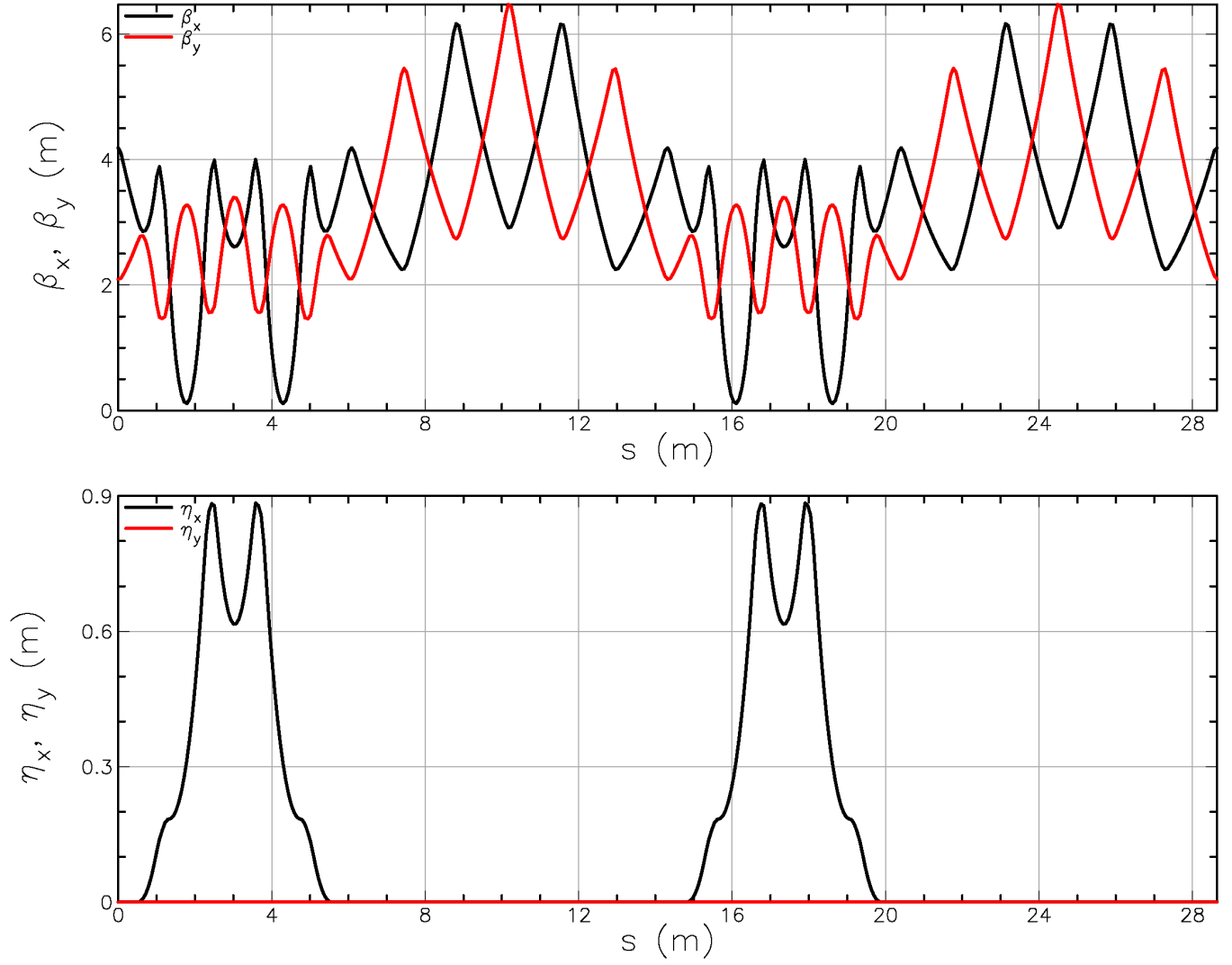


Figure 4: The top plot is of the $\beta_{x,y}$ Twiss functions. The bottom plot is of the $\eta_{x,y}$ dispersion functions.

Table 2: Magnet types used in the RCS damping ring

Element Name	Element Type	Length (m)	B field (T)	B ₁ gradient (Tm ⁻¹)	B ₂ gradient/b ₂ multipole (Tm ⁻²)
edip	Sbend	0.419	-1.2513	4.393	-2.1328 × 10 ⁻³
mdip	Sbend	0.837	-1.2513	3.383	-2.1328 × 10 ⁻³
efq	Quadrupole	0.200		-4.088	
edq	Quadrupole	0.200		0.013	
mfq	Quadrupole	0.100		-16.809	
sqd	Quadrupole	0.200		4.004	
asfq	Sextupole	0.050			-379.429
asf2	Sextupole	0.050			-185.344
ssf	Sextupole	0.050			-134.877
ssd	Sextupole	0.050			11.895
asf3	Sextupole	0.050			-212.524
asf4	Sextupole	0.050			-471.262

considered is $|n| \leq 5$. The values for Q_x , Q_y , and Q_s are obtained by solving quotient of the eigenvalues ($\lambda_{1,3,5}$) and 2π of the DR 6×6 transfer matrix, \mathcal{M}_{DR} . Using the Lie Algebra method [18] the 6×6 symplectic matrix can be described as the *Lie transformation* of integral of the Hamiltonian between s_i and s_f :

$$\mathcal{M}_{DR} = e^{-\int_{s_i}^{s_f} H(\mathbf{x}, s) ds} \quad (22)$$

where s are along the particles trajectory and

$$e^{:f:} \equiv \sum_{k=0}^{\infty} :f:^k / k! \quad (23)$$

A few helpful relations are,

$$\begin{aligned} :f: &\equiv \frac{\partial f}{\partial q} \frac{\partial}{\partial p} - \frac{\partial f}{\partial p} \frac{\partial}{\partial q} \\ :f:g &\equiv \frac{\partial f}{\partial q} \frac{\partial g}{\partial p} - \frac{\partial f}{\partial p} \frac{\partial g}{\partial q} = [f, g] \\ :f:^2 g &= [f, [f, g]] \\ e^{:f:} g &= g + [f, g] + [f, [f, g]]/2! + \dots \end{aligned} \quad (24)$$

where $f(z)$ is any function of q, p . The six dimensional phase space coordinates are written as $\mathbf{x} = (x, p_x, y, p_y, z, p_z)$. And since s_i and s_f are two arbitrary points along s , the beginning and end of the lattice are chosen to give the *one-turn-map*. The condition for symplecticity is as follows,

$$J = \mathcal{M}_{DR} J \mathcal{M}_{DR}^T \quad (25)$$

where J is the 6×6 matrix

$$J = \begin{pmatrix} 0 & 1 & 0 & 0 & 0 & 0 \\ -1 & 0 & 0 & 0 & 0 & 0 \\ 0 & 0 & 0 & 1 & 0 & 0 \\ 0 & 0 & -1 & 0 & 0 & 0 \\ 0 & 0 & 0 & 0 & 0 & 1 \\ 0 & 0 & 0 & 0 & -1 & 0 \end{pmatrix} \quad (26)$$

The Hamiltonian equations are written as the Lie derivative generated by H [19],

$$\dot{x} = [x, H] = - : H : x \quad (27)$$

and if the Hamiltonian is s position (time) independent, then

$$x(s) = \mathcal{M}(s)x^i = e^{-t:H}x^i \quad (28)$$

otherwise (s position/time dependent case)

$$\frac{d}{ds}\mathcal{M}(s) = -(s) : H : \quad (29)$$

A more general description of the transfer matrix may be obtained from [20].

$$\mathcal{M}_{DR} = \begin{pmatrix} A & b & \mathcal{D}_a \\ a & B & \mathcal{D}_b \\ p_1 & p_2 & C \end{pmatrix} \quad (30)$$

Here the elements of the matrix are 2×2 sub-matrices.

- The A and B matrices indicate the focusing of the lattice
- The lower case a and b indicate coupling
- \mathcal{D}_a and \mathcal{D}_b indicate dispersion and time of flight dependence on transverse initial conditions, \mathcal{D}_b specifically coupled dispersion
- C shows changes in path length

The third order sum resonance is close, shown in Fig. 5 the chromatic footprint, but the fractional tune does not cross. Here we will define $\delta = p_z/P_0$ as the momentum spread of the beam. The chromaticities from the natural to third order are shown in Tab. 3. Due to the designed sextupole field of the dipoles, the vertical natural chromaticity is positive.

3.1 The Arc

The maximum β -functions in the arc is 3.88 m, horizontal and 2.71 m vertical. The constraint on the dispersion at the entrance and exit of the arc demands that the horizontal phase advance, ϕ_a , be 2π through the arc.

The \mathcal{M}_{arc} matrix is the concatenated matrix of the sector bend (beam enters and exits perpendicular to the face of the dipole) combined-function dipoles, quadrupoles, sextupoles, and drifts. A dipole map, in the absence of coupling, is written as:

$$\mathcal{M}_d = \begin{pmatrix} \cos \theta & \sin \theta/g & 0 & 0 & 0 & (1 - \cos \theta)/g \\ -g \sin \theta & \cos \theta & 0 & 0 & 0 & \sin \theta \\ 0 & 0 & 1 & \theta/g & 0 & 0 \\ 0 & 0 & 0 & 1 & 0 & 0 \\ -\sin \theta & -(1 - \cos \theta)/g & 0 & 0 & 1 & L_d/(\gamma\beta)^2 - (\theta - \sin \theta)/g \\ 0 & 0 & 0 & 0 & 0 & 1 \end{pmatrix} \quad (31)$$

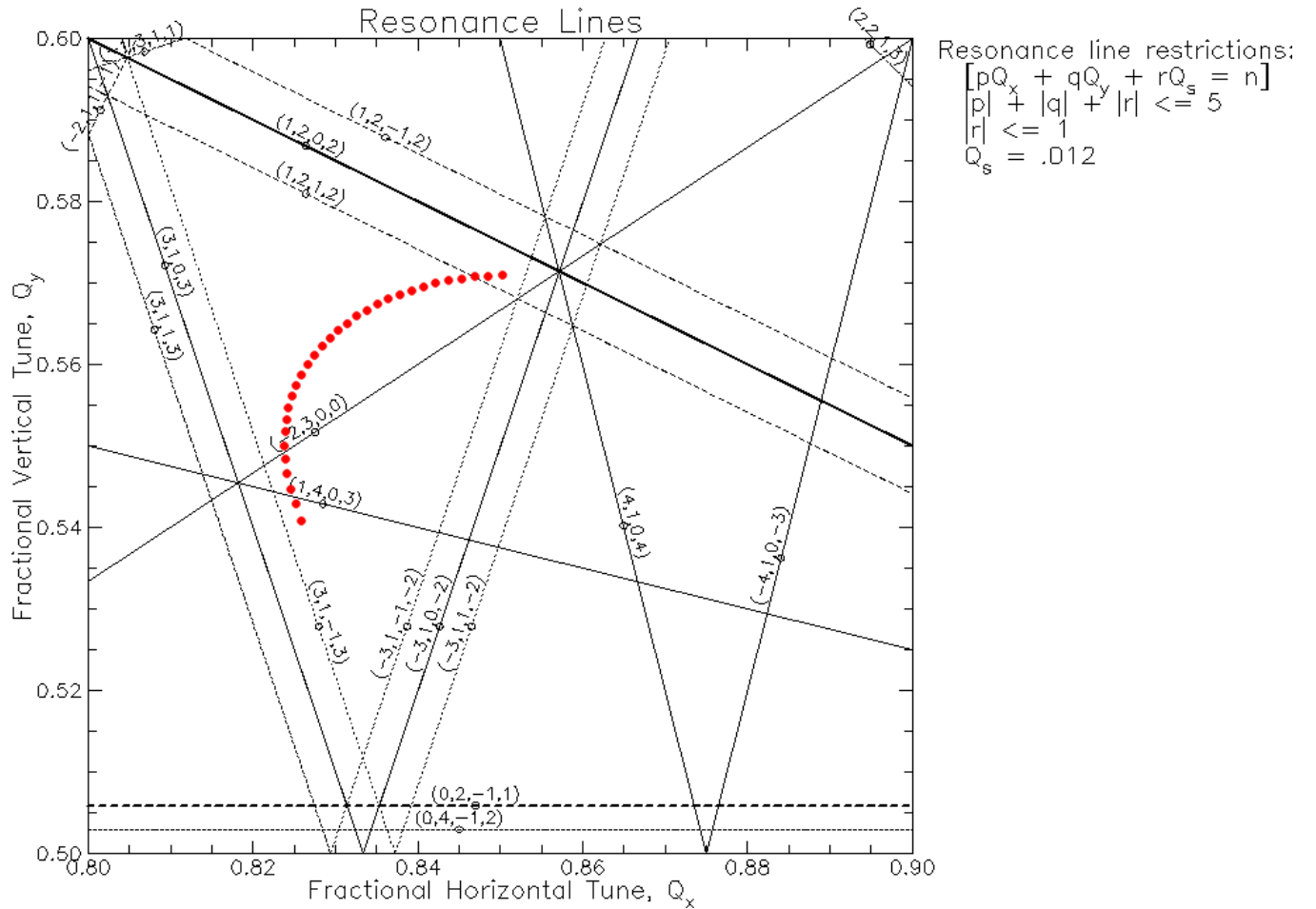


Figure 5: The chromatic footprint of the damping ring with a $\delta \pm 1.5\%$ over a tune space of 0.8 to 0.9 horizontally and 0.5 to 0.6 vertically. The numbers within the parentheses of the tune diagram are read as p, q, r , and n .

In the transfer map Equ. 31, $g = 1/\rho$ is the geometric strength of the dipole (ρ is the bend radius), θ is the bend angle, and L_d is the length of the dipole. To account for the quadrupolar field of the combined-function magnet, an additional map must be included [21, 22]:

$$\mathcal{M}_{x,cf} = \begin{pmatrix} \mathcal{K}\mathcal{S}_y \sin \mathcal{K}_x + \mathcal{C}_y \cos \mathcal{K}_x & -\frac{|K_y|-|K_x|}{2\sqrt{K_y}|K_x|L_d^2} \sinh \mathcal{K}_x \left(\cos \mathcal{K}_x - \frac{|K_y|+|K_x|}{|K_y|-|K_x|} \right) + \frac{1}{\sqrt{K_x}} \cosh \frac{\sqrt{K_y}}{2} \sin \mathcal{K}_x \\ \frac{|K_y|-|K_x|}{2\sqrt{K_y}} \mathcal{S}_y \left(\cos \mathcal{K}_x + \frac{|K_y|+|K_x|}{|K_y|-|K_x|} \right) - \sqrt{K_x} \mathcal{C}_y \sin \frac{\sqrt{K_x} L_d}{2} & \mathcal{K}\mathcal{S}_y \sin \mathcal{K}_x + \cosh \mathcal{K}_y \cos \mathcal{K}_x \end{pmatrix} \quad (32)$$

$$\mathcal{M}_{y,cf} = \begin{pmatrix} \mathcal{K} \sin \frac{\sqrt{K_x}}{L_d} 2\mathcal{S}_y + \cos \mathcal{K}_x \mathcal{C}_y & -\frac{|K_y|-|K_x|}{2\sqrt{K_x}|K_y|L_d^2} \sin \mathcal{K}_y \left(\mathcal{C}_y - \frac{|K_x|+|K_y|}{|K_x|-|K_y|} \right) + \frac{1}{\sqrt{K_y}} \cos \frac{\sqrt{K_x}}{2} \mathcal{S}_y \\ \sqrt{K_x} \sin \mathcal{K}_x \left(\sin \frac{|K_y|}{|K_x|} \sinh^2 \frac{\sqrt{K_y}}{4} - \cosh^2 \frac{\sqrt{K_y}}{4} \right) + \sqrt{K_y} \cos \frac{\sqrt{K_x}}{2} \sinh \frac{\sqrt{K_x}}{2} & \mathcal{K} \sin \mathcal{K}_x \mathcal{S}_y + \cos \mathcal{K}_x \mathcal{C}_y \end{pmatrix} \quad (33)$$

where $\mathcal{K}_{x,y} = \frac{\sqrt{K_{x,y}} L_d}{2}$, $\mathcal{S}_{x,y} = \sinh \frac{\sqrt{K_{x,y}} L_d}{2}$, $\mathcal{C}_{x,y} = \cosh \frac{\sqrt{K_{x,y}} L_d}{2}$, and $\mathcal{K} = \frac{|K_y|-|K_x|}{2\sqrt{K_x}\sqrt{K_y}}$. The complete transfer map of the combined-function magnet becomes:

$$\mathcal{M}_{cf} = M_d + \begin{pmatrix} \mathcal{M}_{x,cf} & 0 & 0 \\ 0 & \mathcal{M}_{y,cf} & 0 \\ 0 & 0 & M_z \end{pmatrix} \quad (34)$$

These combined function magnets increase the damping partition, a more complete description of the radiation integrals for bending magnets with quadrupolar field gradients can be found [23]. M_z is the description of longitudinal rotation

$$M_z = \begin{pmatrix} 1 & L_d/(\gamma\beta)^2 \\ 0 & 1 \end{pmatrix} \quad (35)$$

The $K_{x,y}$ value is the normalized strength of the quadrupole which is the field gradient, $(\partial B_{y,x}/\partial B_{x,y})$, of the quadrupole normalized to the rigidity, $B_0\rho = p/q_{charge}$. The quadrupole transfer map is:

$$\mathcal{M}_q = \begin{pmatrix} \cos \sqrt{K_x} L_q & \sin \sqrt{K_x} L_q / \sqrt{K_x} & 0 & 0 & 0 & 0 \\ -\sqrt{K_x} \sin \sqrt{K_x} L_q & \cos \sqrt{K_x} L_q & 0 & 0 & 0 & 0 \\ 0 & 0 & \cosh \sqrt{K_y} L_q & \sinh \sqrt{K_y} L_q / \sqrt{K_y} & 0 & 0 \\ 0 & 0 & \sqrt{K_y} \sinh \sqrt{K_y} L_q & \cosh \sqrt{K_y} L_q & 0 & 0 \\ 0 & 0 & 0 & 0 & 1 & L_q/(\gamma\beta)^2 \\ 0 & 0 & 0 & 0 & 0 & 1 \end{pmatrix} \quad (36)$$

. L_q is the effective length of the quadrupole. Since we assume that the beam is on axis, there will be no contribution from the sextupoles on the linear optics. We treat the sextupoles as a drift with the drift transfer map:

$$\mathcal{M}_{drift} = \begin{pmatrix} 1 & L & 0 & 0 & 0 & 0 \\ 0 & 1 & 0 & 0 & 0 & 0 \\ 0 & 0 & 1 & L & 0 & 0 \\ 0 & 0 & 0 & 1 & 0 & 0 \\ 0 & 0 & 0 & 0 & 1 & L/(\gamma\beta)^2 \\ 0 & 0 & 0 & 0 & 0 & 1 \end{pmatrix} \quad (37)$$

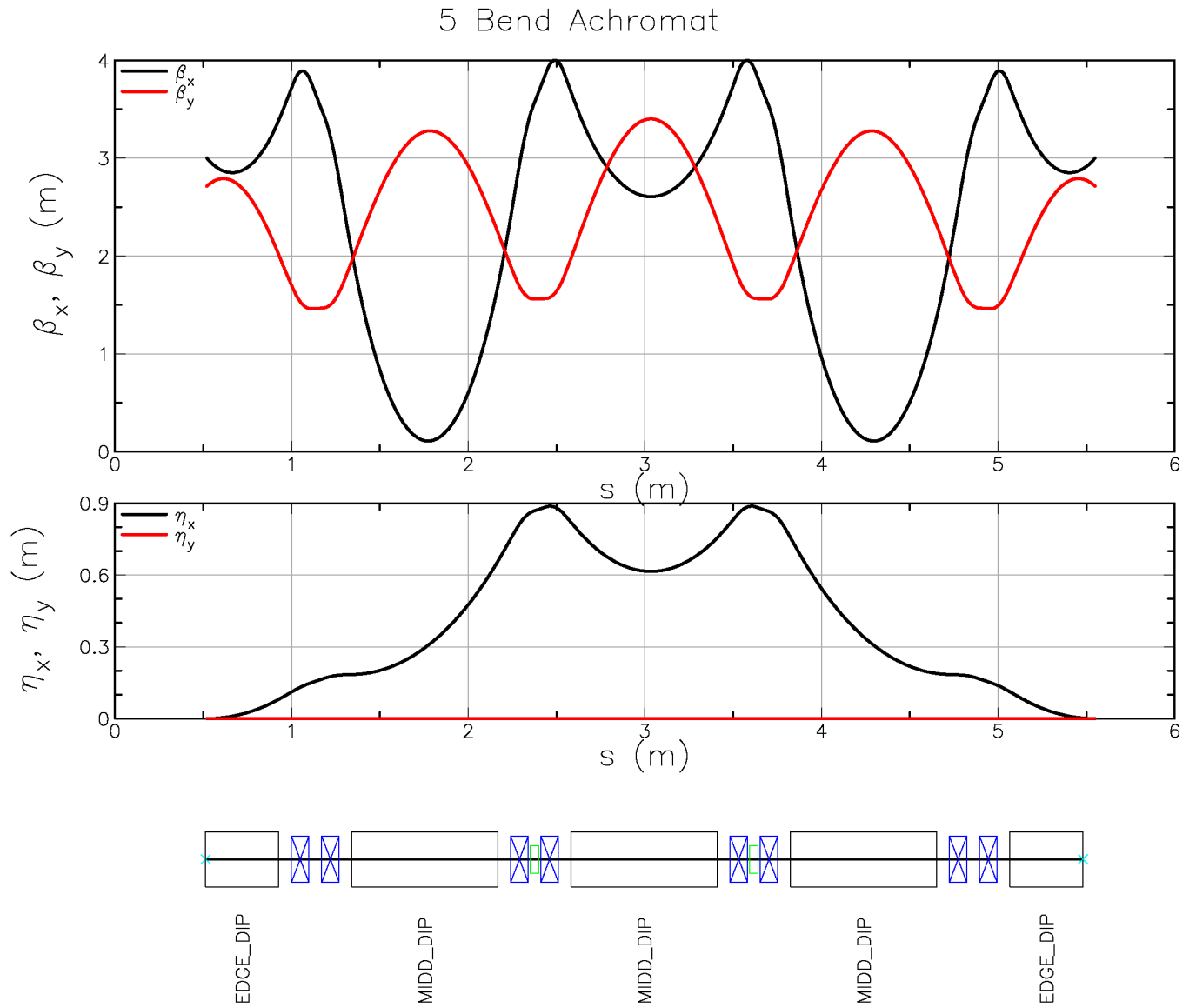


Figure 6: The top plot is of the $\beta_{x,y}$ functions. The middle plot is of the $\eta_{x,y}$ functions. The bottom plot is the lattice layout where the black box:dipole, blue xbox:quarupole, and the green box:sextupole.

From these maps we can now write the complete map of the arc as:

$$\mathcal{M}_{arc} = \mathcal{M}_{1 \leftarrow 31} \quad (38)$$

. The \mathcal{M}_{arc} is the concatenation of 31 elements.

3.2 The Straight Section

Figure 7 shows the optics of the straight section. It is composed of simple FODO cells with two families of harmonic sextupoles that do not affect the linear chromaticity and are used to control the resonance driving terms. One of the straight sections will contain the RF system for the the DR. The other straight will contain the injection system from the 400 MeV LINAC.

The beam will be injection from the LINAC through the spin rotator [24] and into the DR. The LINAC will inject a total of 4 bunches of 7 nC into the DR. Many different methods [25, 26] are available for injection into the DR. The injection method most favorable for the DR is *longitudinal injection*, where a septum and a short pulsed kicker places the slightly higher momentum beam onto a closed orbit of higher momentum. The beam then damps to the equilibrium orbit. The benefit is a closed orbit bump is unnecessary.

3.2.1 Longitudinal Dynamics

If we consider the longitudinal electric field from the radiofrequency cavities, we will need to revisit Equ. 3. The longitudinal electric field is described by [27, 28], however to remain consistent and keeping s dependence of the Hamiltonian, we write the electric field along the s coordinate as [29]:

$$\begin{aligned} E_s &= -\frac{\partial A_s}{\partial t} \\ &= \sum_i V_i \delta_p(s - s_i) \sin(\omega_{rf}t + \phi_{0i}) \end{aligned} \quad (39)$$

where number of cavities is i , with a voltage gain of V_i located at $s = s_i$. The angular frequency is $\omega_{rf} = h\omega_{rev}$, ϕ_{0i} is the initial phase, and δ_p is a periodic delta function with the circumference being the period. The RF cavity harmonic, h , and the revolution frequency, ω_{rev} are listed in Tab. 1. The vector potential can be:

$$A_s = \sum_i \frac{V_i}{\omega_{rf}} \delta_p(s - s_i) \cos(\omega_{rf}t + \phi_{0i}) \quad (40)$$

From this point with the help of a canonical transformation, the synchrotron Hamiltonian for electrons is [30, 31],

$$\begin{aligned} H_{syn} &= -\frac{1}{2} \left(\frac{\eta_x}{\rho} - \frac{1}{\gamma^2} \right) \delta^2 \\ &\quad - \sum_i \frac{eV_i}{h\beta^2 E} \delta_p(\theta - \theta_i) (\cos(\phi + \phi_{0i}) + \phi \sin(\phi_{0i})) \end{aligned} \quad (41)$$

where the βc is the speed, γ is the Lorentz factor, and E is the energy of the particle. Here $\phi = \omega_{rf}t$ is the RF phase relative to ϕ_s . The total Hamiltonian becomes the sum of H (Equ. 15), and H_{syn} .

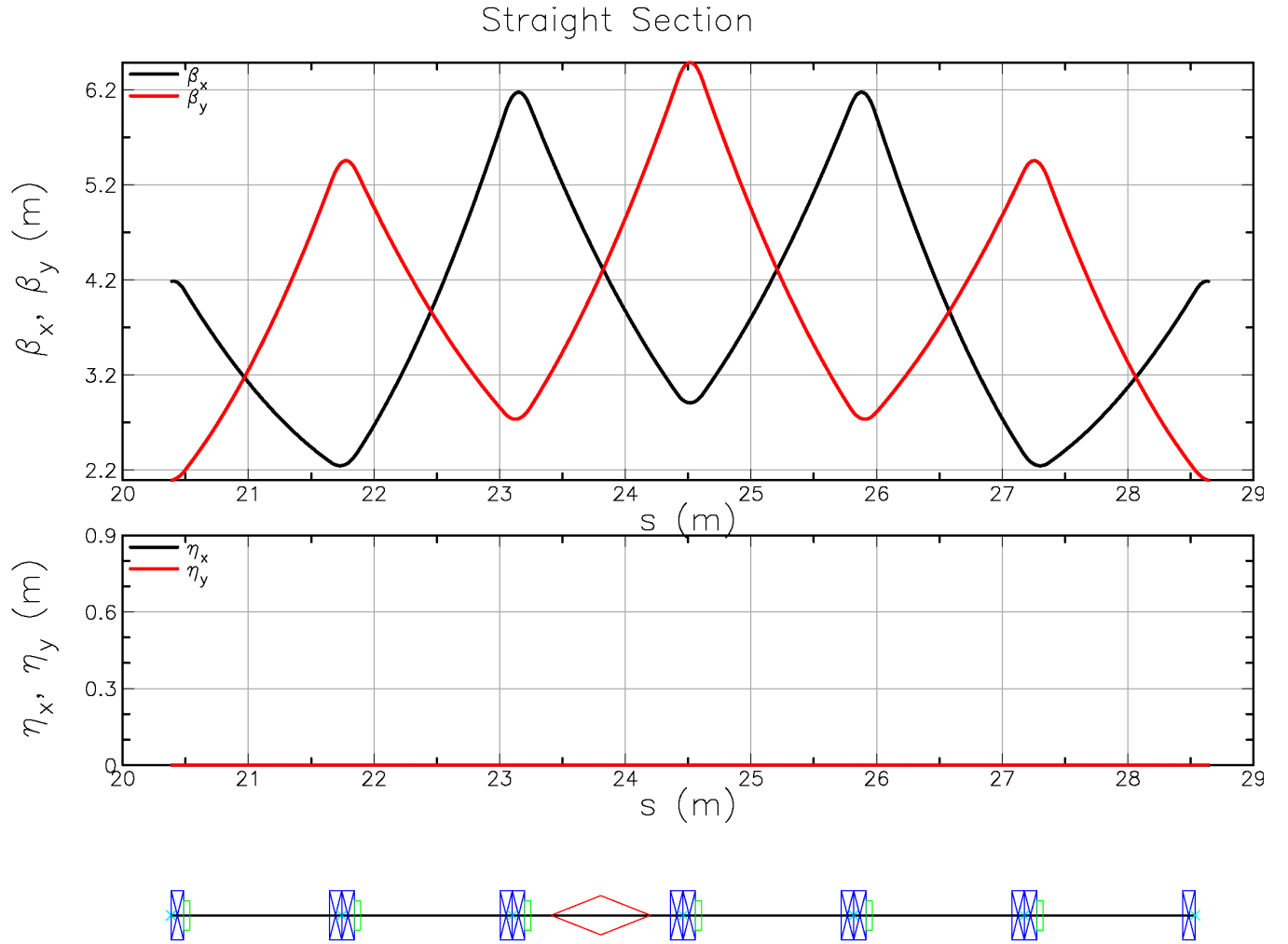


Figure 7: The top plot is of the $\beta_{x,y}$ Twiss functions. The middle plot is of the $\eta_{x,y}$ dispersion functions. The bottom plot is the lattice layout where the black box:dipole, blue xbox:quarupole, and the green box:sextupole. The diamond:red indicates the position of the RF cavity.

4 Dynamic Aperture

The dynamic aperture is the stable region within phase space after a large number of applications of the map, \mathcal{M} , onto a set of coordinates, \mathbf{x} . The chromaticities, as mentioned in a previous section, is to shown in Tab. 3. The first, second, and third order chromaticities are:

Table 3: Damping ring chromaticities up to third order

Chromatic Order	Horizontal	Vertical
Natural	-11.50	6.24
Linear	0.98	0.98
Second	37.79	-32.49
Third	-850.0	79.98

$$\begin{aligned}\zeta_{x,y}^{(1)} &= \frac{\partial Q_{x,y}}{\partial \delta} \\ \zeta_{x,y}^{(2)} &= \frac{\partial^2 Q_{x,y}}{\partial \delta^2} \\ \zeta_{x,y}^{(3)} &= \frac{\partial^3 Q_{x,y}}{\partial \delta^3}\end{aligned}\quad (42)$$

If we have $\nu = |p, q|/|n|$ of Equ. 21, then we consider the particle motion to resonate on a p^{th} or

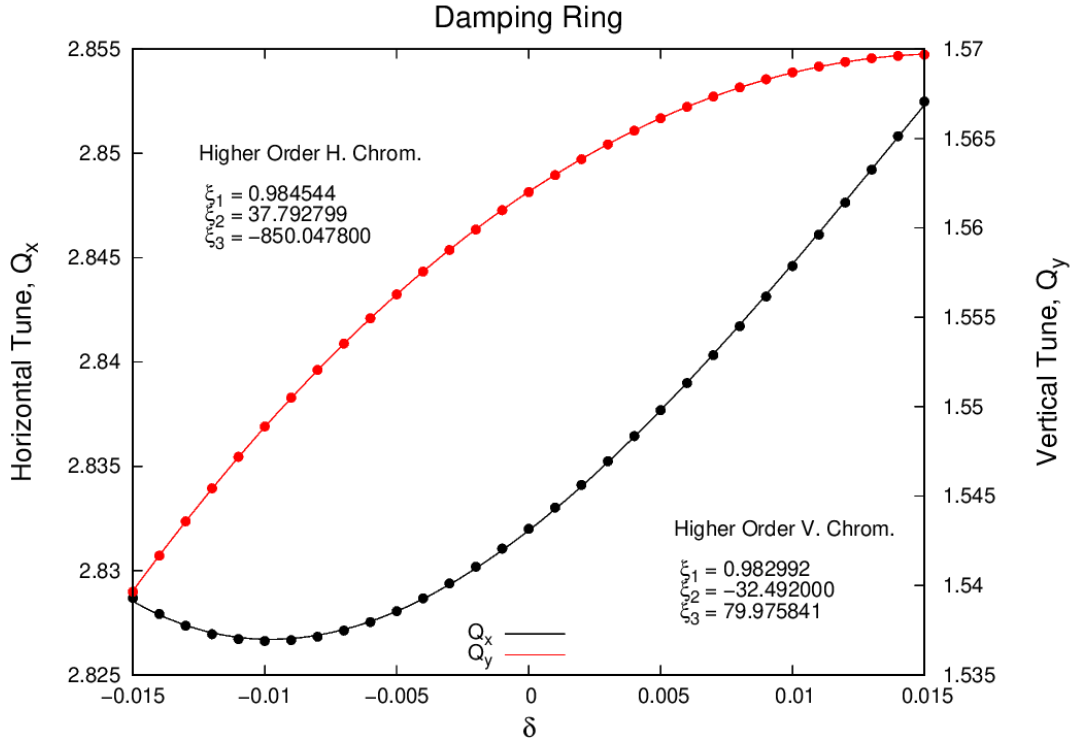


Figure 8: A scan of the horizontal and vertical tune over $\pm 1.5\%$ momentum deviation

q^{th} harmonic n^{th} order (integer) resonance [32, 33]. The KAM-Theory describes the position of the stability border of a the non-integrable perturbed Hamiltonian system. The theorem states

that if the perturbation is small and the frequencies of the Hamiltonian are incommensurate, the motion is confined to an N -torus. The exception is the negligible set of initial conditions that result in meandering trajectories on the energy surface [34]. As the order increases, the resonance strength decreases. The separatrix may be defined here as the border trajectory between rotation and oscillation which separates motions of different type. If separatrices begin to touch each other, the resonances begin to overlap. The motion about overlapping resonances are unstable and are called stochastic oscillations/instability, see Appendix D.

Through normalizing the coordinates transformation into *action-angle* variable, J, ϕ , found in Appendix B, the general n -D integrable system with a perturbation in which the Hamiltonian is a function of its angle has the form

$$H(J, \psi) = H_0(J) + \epsilon H_p(J, \psi) \quad (43)$$

where $\epsilon H_p(J, \psi)$ describe the external perturbation.

4.1 Optimization

To describe the optimization of the dynamic aperture, we use the resonance base that is defined in Appendix C to define the resonance driving terms (RDT). We define the Lie generator as h : [35, 36]:

$$h_{ijklm} \equiv A_{ijklm} e^{i\phi_{ijklm}} \quad (44)$$

where A_{ijklm} and ϕ_{ijklm} are the amplitude and phase of the RDT. The first order driving terms that drive linear chromaticity are:

$$\begin{aligned} h_{11001} &= \frac{1}{4} \sum_{i=1}^N [(k_1 L)_i - 2(k_2 L)_i \eta_{xi}^{(1)}] \beta_{xi} + \mathcal{O}(\delta^2) \\ h_{00111} &= -\frac{1}{4} \sum_{i=1}^N [(k_1 L)_i - 2(k_2 L)_i \eta_{xi}^{(1)}] \beta_{yi} + \mathcal{O}(\delta^2) \end{aligned} \quad (45)$$

where k_1 and k_2 are the normalized strengths of the quadrupole and sextupole, respectively. L is the length of the slice of the lattice at that moment.

$$\begin{aligned} h_{20001} &= \frac{1}{8} \sum_{i=1}^N [(k_1 L)_i - 2(k_2 L)_i \eta_{xi}^{(1)}] \beta_{xi} e^{2i\phi_{xi}} + \mathcal{O}(\delta^2) \\ h_{00201} &= -\frac{1}{8} \sum_{i=1}^N [(k_1 L)_i - 2(k_2 L)_i \eta_{xi}^{(1)}] \beta_{yi} e^{2i\phi_{yi}} + \mathcal{O}(\delta^2) \\ h_{10002} &= \frac{1}{8} \sum_{i=1}^N [(k_1 L)_i - 2(k_2 L)_i \eta_{xi}^{(1)}] \eta_{xi} \sqrt{\beta_{xi}} e^{2i\phi_{xi}} + \mathcal{O}(\delta^2) \end{aligned} \quad (46)$$

We also have that complex conjugates $h_{20001} = h_{02001}^*$, $h_{00201} = h_{00201}^*$, and $h_{10002} = h_{01002}^*$. The synchrotron resonances are driven by h_{20001} and h_{00201} . The second order dispersion is driven by h_{10002} . Equations 45 and 46 are known as *chromatic terms* due to their dependence on dispersion. The first order geometric terms that are independent of the dispersion and with frequencies $p = 1$, $p = 3$, and $p = 1, q = \pm 2$ drive the betatron modes are listed in Equation 97 of [35]. A more comprehensive list of driving terms can be found in [37]. Table 4 lists all the driving

terms used in the optimization. The goal of the optimization is to minimize the absolute value of the first and second order terms and the real component of the terms h_{22000} , h_{11110} , and h_{00220} which drive the amplitude dependent tune shift.

Table 4: Summed resonance driving terms used in optimization and there value

Term	Resonance Strength
h_{20001}	4.293213915535
h_{00201}	0.619985917889
h_{10002}	1.671614484610
h_{21000}	3.853470780730
h_{30000}	4.530626940065
h_{10110}	2.482651709279
h_{10020}	4.200984095308
h_{10200}	5.641184353058
h_{22000}	200.2780397596
h_{11110}	214.4308899946
h_{00220}	2.735127566092
h_{31000}	239.5874528930
h_{40000}	200.9172734928
h_{20110}	141.8863601545
h_{11200}	71.60543118530
h_{20020}	111.6841084502
h_{20200}	42.65041090370
h_{00310}	47.28542658925
h_{00400}	33.10986649867

In addition to the RDTs, the chromatic perturbations described in Appendix E must be corrected. These W functions show the $\beta_{x,y}$ -beating that occurs due to the momentum spread of the beam. By minimizing the absolute value of the functions, the momentum aperture of the lattice improves which in turn allows a dynamic aperture to be found at higher momenta. Figure 9 shows the W functions for each element of the DR.

The dynamic aperture in physical space after optimization is shown in Fig. 10. The beam sizes, σ_x and σ_y at the location of observation are 0.462 mm and 0.327 mm, respectively. The solid black line of the plot indicated the aperture of the beam pipe, 32.9 mm inner diameter. The dynamic aperture is scanned by the process of increasing the orbital amplitude of the tracked particle for 282497 turns which is the turns within two damping periods. Synchrotron oscillations, radiation damping, and stochastic radiation fluctuations are included within the tracking. A total of 30 evenly spaced phase angles were taken over a 180° span. The total number of sextupole families in the DR is six, where each arc has two sextupole families.

5 Radiation Damping

The DR is designed to minimize the momentum spread of the beam before injection into the RCS. The energy loss per turn, U_0 is

$$U_0 = \frac{2r_c E_0^4}{3(mc^2)^3} I_2 \quad (47)$$

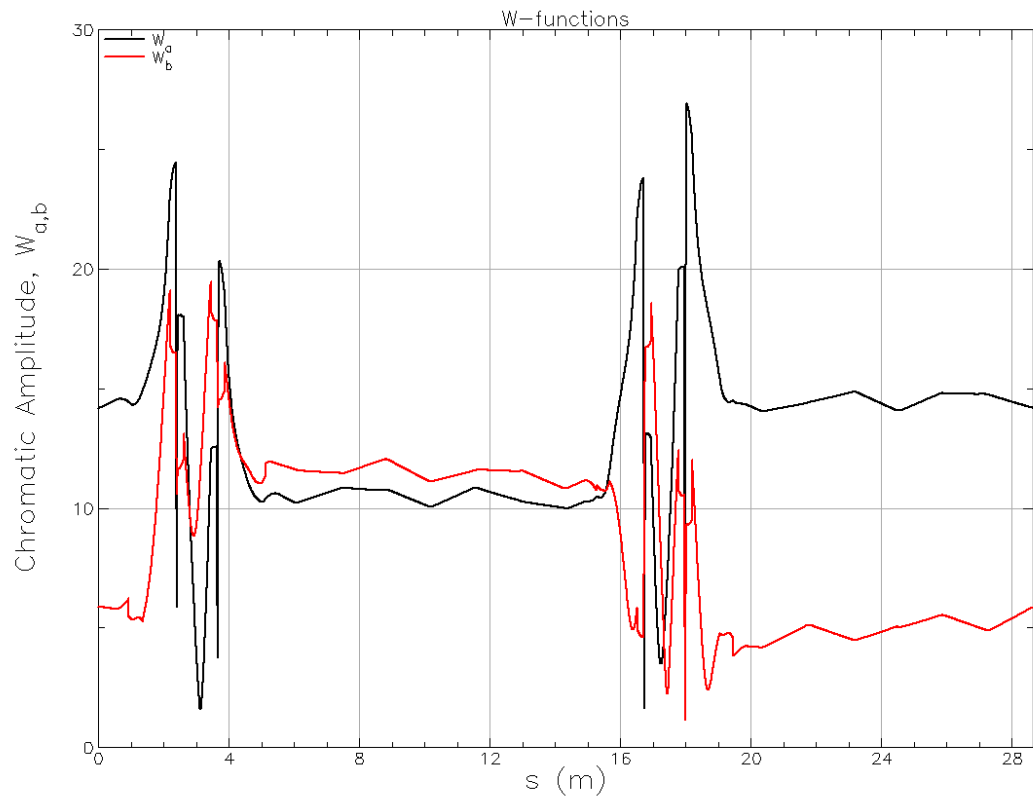


Figure 9: The W-function for the DR. Black:horizontal and red:vertical.

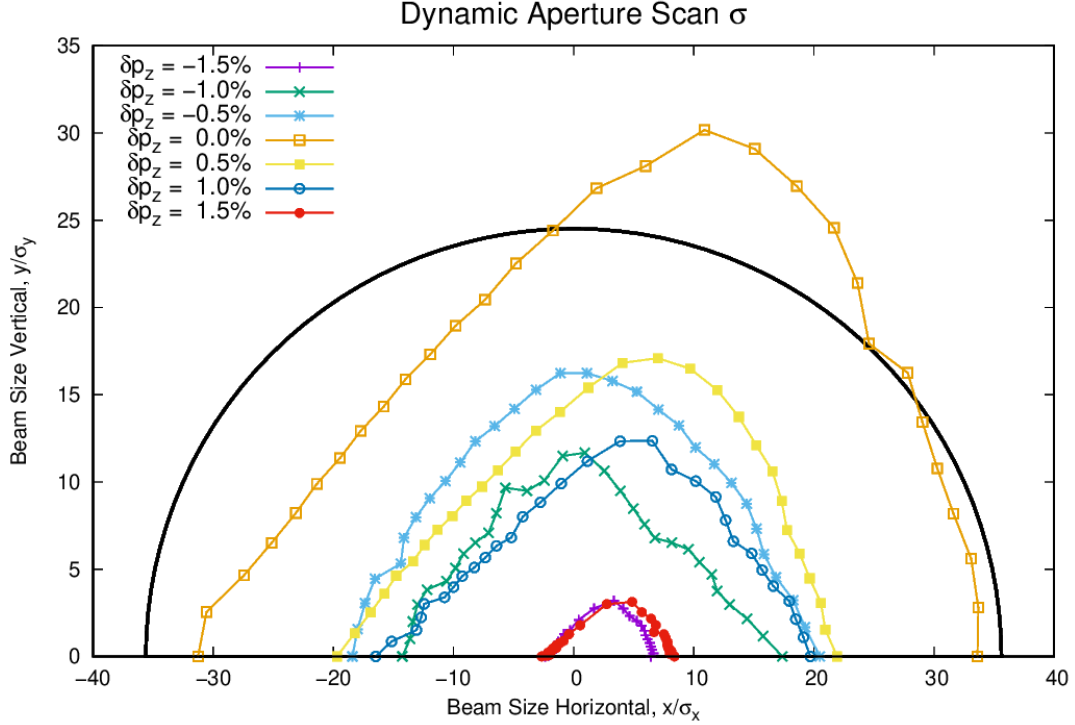


Figure 10: Dynamic Aperture scan from $\pm 1.5\%$ δ . 1.5% is 3σ of the injected beam momentum spread. The solid black semicircle beam pipe aperture radius at 35.6σ

where r_c is the classical electron radius, mc^2 is the rest mass energy, and E_0 is the nominal stored energy. The equilibrium emittances and energy spread are calculated using Equ. 16:

$$\begin{aligned} \epsilon_x &= \frac{C_q}{I_2 - I_{4a}} \gamma_0 I_{5a} \\ \sigma_p &= \frac{\sigma_E}{E_0} = \gamma_0 \sqrt{C_q \frac{I_3}{2I_2 + I_{4z}}} \end{aligned} \quad (48)$$

where I_{4z} is

$$I_{4z} = \int_0^C (G^2 + 2K_{x,y}) G \eta ds \quad (49)$$

and $C_q = 3.832 \times 10^{-13}$. The transverse and longitudinal damping for the electrons over a ± 40 MeV energy range can be summarized in Tab. 5. The damping times are found using

$$\begin{aligned} \tau_x &= \frac{2pc}{J_x E_f \omega_{rev}} \\ \tau_y &= \frac{2pc}{J_y E_f \omega_{rev}} \\ \tau_z &= \frac{2pc}{J_z E_f \omega_{rev}} \end{aligned} \quad (50)$$

with J_x , J_y , and J_z are the partition numbers that show the distribution of damping in the three degrees of freedom of system and E_f is the final energy after one turn. The inverse of these

damping time are known as the damping coefficients, α_i . The partition numbers are

$$J_x = 1 - \frac{I_{4a}}{I_2}, \quad J_y = 1 - \frac{I_{4b}}{I_2}, \quad J_z = 2 + \frac{I_{4z}}{I_2} \quad (51)$$

For tracking, a fifth order map of the DR is generated. The projected beam sizes and momentum spread from a tracked bunch at 400 MeV after four damping periods are shown in Fig. 11 and Fig. 12. It is clear that within the first damping period the beam sizes and momentum spread are reduced. The *stochastic radiation fluctuations*, which prevents the vertical emittance of the beam from becoming zero [38], is calculated while tracking 1000 particles. Over a 180 ms, twenty damping periods, is shown in Fig. 13 and Fig. 14. The tracking results show emittance blowup with the first three damping periods which can be prevented by avoiding the fifth order sum resonance. From the tracking results, over 87% of the beam survives for the twenty damping periods. Further study is needed to include the intensity dependent collective effects such as intrabeam scattering [39]. The RCS has a dynamic range of 45 which at a 400 MeV injection

Table 5: The damping times of the DR with respect to varying energy

Energy (MeV)	γ	Turns	τ_x (ms)	τ_y (ms)	τ_z (ms)	ϵ_x nm
364	712.33023082	124958.16	18.4984	47.7527	114.0908	34.3787
368	720.15803555	120927.74	17.9018	46.2124	110.4087	35.1385
372	727.98584028	117068.78	17.3306	44.7377	106.8833	35.9066
376	735.81364502	113372.28	16.7834	43.3251	103.5065	36.683
380	743.64144975	109829.79	16.259	41.9713	100.2705	37.4677
384	751.46925449	106433.35	15.7562	40.6733	97.168	38.2607
388	759.29705922	103175.53	15.274	39.4283	94.1922	39.062
392	767.12486396	100049.32	14.8112	38.2336	91.3367	39.8716
396	774.95266869	97048.15	14.3669	37.0867	88.5955	40.6895
400	782.78047342	94165.82	13.9403	35.9852	85.9629	41.5158
404	790.60827816	91396.5	13.5303	34.9269	83.4335	42.3503
408	798.43608289	88734.72	13.1363	33.9097	81.0025	43.1931
412	806.26388763	86175.31	12.7574	32.9316	78.665	44.0442
416	814.09169236	83713.39	12.393	31.9908	76.4166	44.9037
420	821.91949709	81344.36	12.0423	31.0854	74.253	45.7714
424	829.74730183	79063.88	11.7047	30.2139	72.1704	46.6475
428	837.57510656	76867.85	11.3796	29.3747	70.165	47.5318
432	845.4029113	74752.4	11.0664	28.5663	68.2331	48.4245
436	853.23071603	72713.88	10.7647	27.7872	66.3716	49.3254
440	861.05852077	70748.8	10.4738	27.0363	64.5772	50.2347

energy experiences additional magnetic field errors due to the field at 400 MeV not being well defined. The damping ring, theory, can also serve as a booster to the RCS to energies up to 1 GeV. This will require that the DR in its current configuration to utilize superconducting dipole magnets. Appendix F gives a discussion on the feasibility of the DR being used as a booster to the RCS.

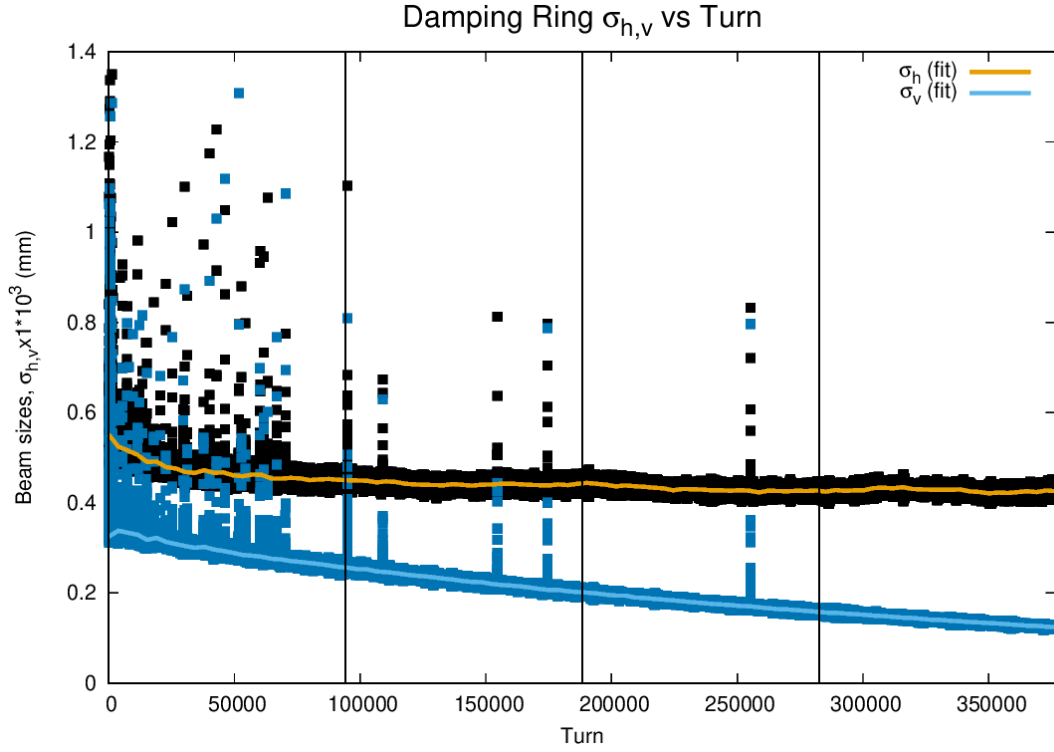


Figure 11: The projected transverse beam sizes from a tracked beam four damping periods. In the tracking model, radiation fluctuations are included. The initial beam sizes at the observation point, where $\beta_{x,y} = (4.18, 2.09)$ m, are $\sigma_{h_i, v_i} = (0.46, 0.33)$ mm. The beam sizes after one damping period $\sigma_{h_1, v_1} = (0.44, 0.25)$ mm, two damping periods $\sigma_{h_2, v_2} = (0.44, 0.20)$ mm., three damping periods $\sigma_{h_3, v_3} = (0.43, 0.16)$ mm and four damping periods $\sigma_{h_4, v_4} = (0.42, 0.12)$ mm

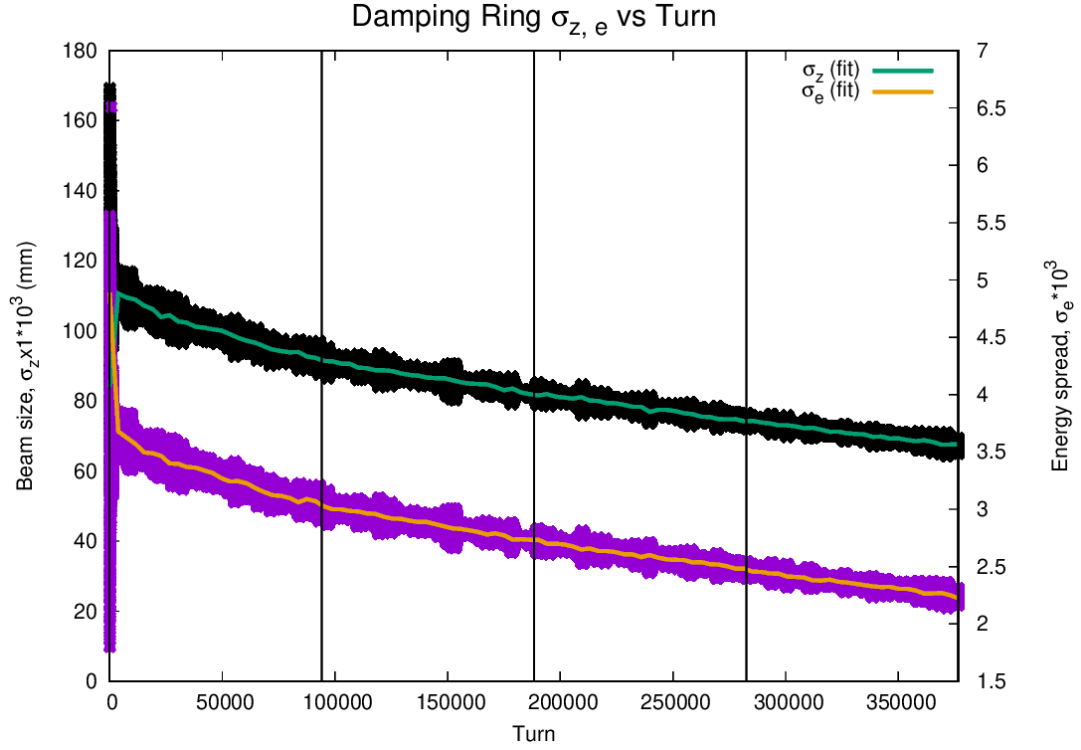


Figure 12: The projected bunch length and energy spread from a tracked beam four damping periods. In the tracking model, radiation fluctuations are included. The initial bunch length is $\sigma_{zi} = 54$ mm and the energy spread, $\sigma_e = \beta^2 \delta$, is initially $\sigma_{ei} = 5.56 \times 10^{-3}$. The bunch length after one damping period is $\sigma_{z1} = 91$ mm, after two $\sigma_{z2} = 82$ mm, after three $\sigma_{z3} = 72$ mm, and after four $\sigma_{z4} = 69$ mm. The energy spread after one damping period is $\sigma_{e1} = 3.1 \times 10^{-3}$, after two $\sigma_{e2} = 2.7 \times 10^{-3}$, after three $\sigma_{e3} = 2.5 \times 10^{-3}$ and after four $\sigma_{e4} = 2.2 \times 10^{-3}$.

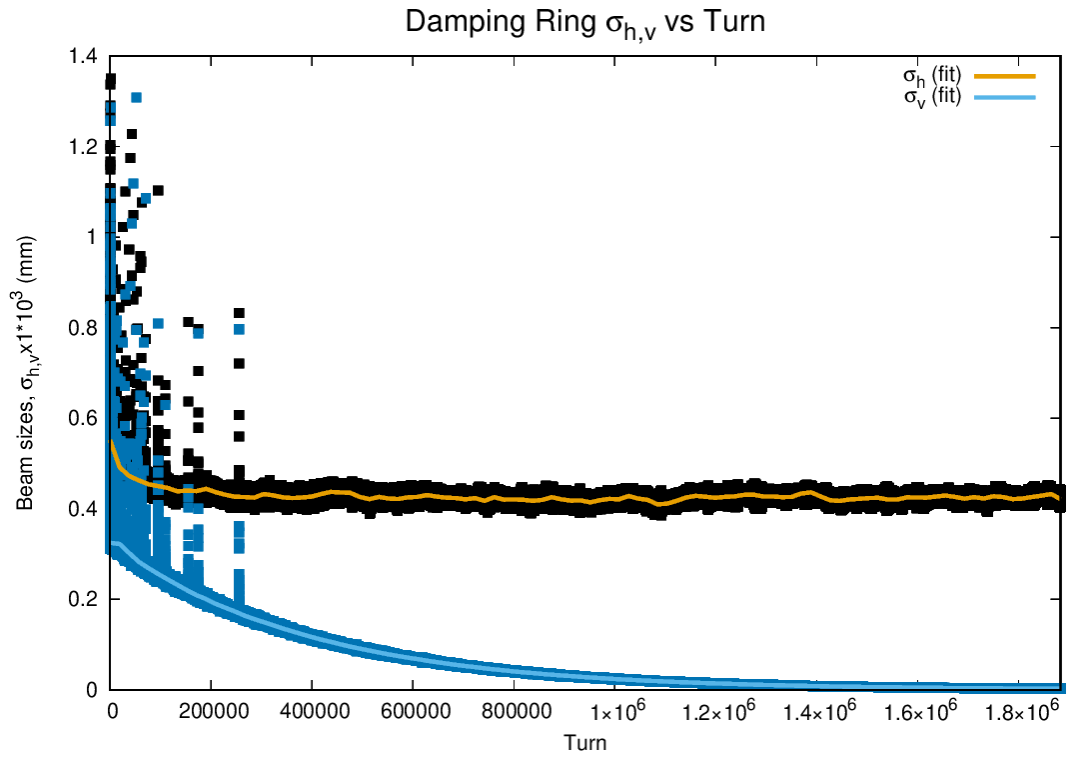


Figure 13: The projected transverse beam sizes from a tracked beam twenty damping periods. In the tracking model, radiation fluctuations are included. The initial beam sizes at the observation point, where $\beta_{x,y} = (4.18, 2.09)$ m, are $\sigma_{hi,vi} = (0.46, 0.33)$ mm. The final beam sizes are $\sigma_{hf,vf} = (0.41, 2.4 \times 10^{-3})$ mm.

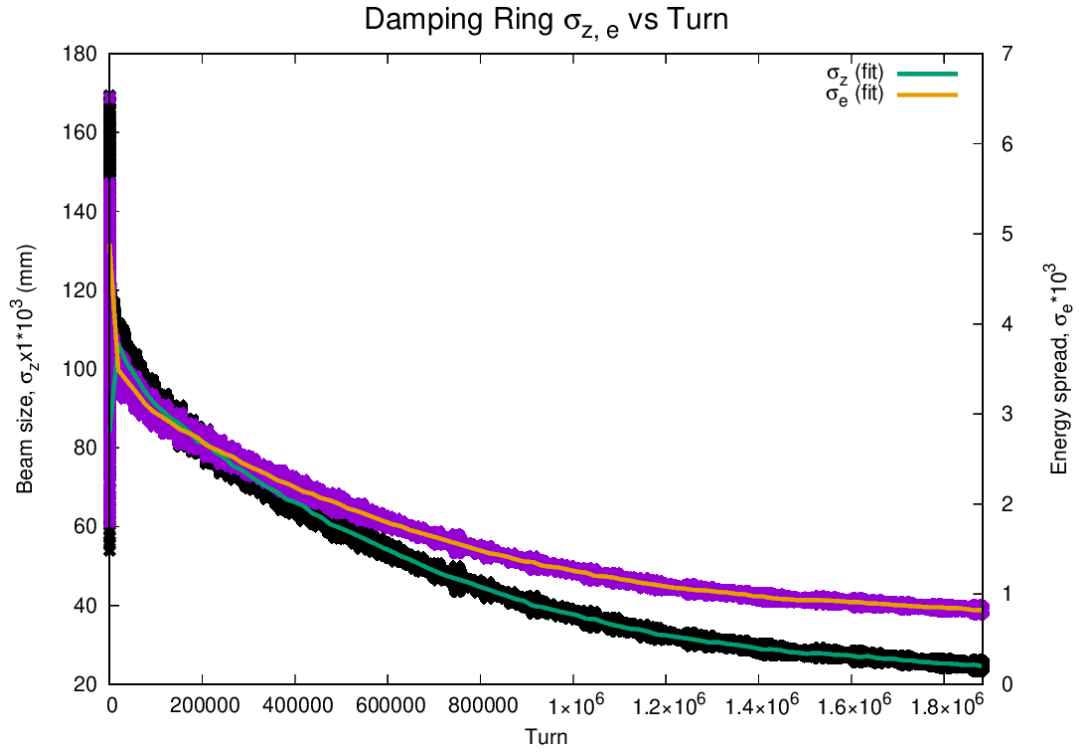


Figure 14: The projected bunch length and energy spread from a tracked beam twenty damping periods. In the tracking model, radiation fluctuations are included. The initial bunch length is $\sigma_{zi} = 54$ mm and the final $\sigma_{zi} = 25$ mm. The energy spread, $\sigma_e = \beta^2 \delta$, is initially $\sigma_{ei} = 5.56 \times 10^{-3}$. The final energy spread is $\sigma_{ef} = 0.81 \times 10^{-3}$.

6 Conclusion

The RCS damping ring is presented. The damping times at 400 MeV, $\tau_x = 13.9403$ ms, $\tau_y = 35.9852$ ms, and $\tau_z = 85.9629$ ms were found. The projected emittances after tracking a single damping period are $\epsilon_x = 46.9$ nm, $\epsilon_y = 3.1$ nm, and $\epsilon_z = 280.65 \mu\text{m}$. The difference in the natural emittance calculated by the synchrotron radiation integrals, and the tracked beam is due to the use of combined function magnets used in the lattice. The horizontal emittance and bunch length are within 13% of the natural emittance and bunch length. The energy spread has a percent difference of 74% which is due to inclusion of the RF system. However, after 4 damping periods, the horizontal emittance is $\epsilon_x = 42.0$ nm which is a less than 1% difference in the emittance calculated by the radiation integrals. The energy spread after 7 damping periods has a percent difference of less than 2%.

7 Acknowledgments

We thank the RCS injector group for the initial inspiration on designing the DR. We thank C. Nieves-Rosada for his extensive work with blender to produce the 3D model of Fig. 1. We thank S. Peggs for his wonderful discussion on the DR.

A Lattice File (damping_ring.bmad: dr-indi-arc.var)

```
parameter[lattice]      = "RCS damping ring"
parameter[geometry]    = closed

parameter[e_tot]        = .4e9
parameter[particle]     = Electron
parameter[n_part]       = 1.74762254084901367E+11 ! full current

bmad_com[max_aperture_limit] = 0.04/2
bmad_com[rel_tol_tracking]   = 1E-3
bmad_com[abs_tol_tracking]   = 1E-6
bmad_com[taylor_order]      = 3
bmad_com[auto_bookkeeper]    = F
bmad_com[csr_and_space_charge_on] = f
bmad_com[spin_tracking_on]   = T
bmad_com[radiation_damping_on] = t
bmad_com[radiation_fluctuations_on] = t
bmad_com[absolute_time_tracking] = T

!-----
!-----
!--Constants
deg_to_rad = pi/180
rigidity=1.334255292039262
!~~cell parameters
arc_radius = 1.75
ndipole=8
bend_ang=((2*pi)/ndipole)
quad_length= .2
sex_length= 0.05!.2
drift_length=quad_length*1.1
!-----
dipole_length=(arc_radius*abs(sin(bend_ang)))-(2*quad_length)
focal_length = dipole_length/sqrt(2)
!-----
cell_length = 2*dipole_length+2*quad_length+4*drift_length
!-----
beginning[beta_a]   = 9
beginning[beta_b]   = 2
!-----
! cfms
!-----
edge_dip:sbend,L=dipole_length/2,ang=bend_ang/2!,k2=-17.1/rigidity
mid_dip:sbend,L=dipole_length,ang=bend_ang!,k2=-17.1/rigidity

edge_fquad:quadrupole,l=quad_length/2
edge_dquad:quadrupole,l=quad_length/2

mid_fquad:quadrupole,l=quad_length/2
mid_dquad:quadrupole,l=quad_length/2

arc_sf1:sextupole,l=sex_length,superimpose,ref = beginning, offset = 2.442822-drift_length/6,
        ref_origin = beginning, ele_origin = center
arc_sf2:sextupole,l=sex_length,superimpose,ref = beginning, offset = 3.700259-drift_length/6,
        ref_origin = beginning, ele_origin = center

arc_sf3:sextupole,l=sex_length,superimpose,ref = beginning, offset = 16.763653-drift_length/6,
```

```

                ref_origin = beginning, ele_origin = center
arc_sf4:sextupole,l=sex_length,superimpose,ref = beginning, offset = 18.021090-drift_length/6,
                ref_origin = beginning, ele_origin = center

!arc_sex:overlay={arc_sf1[k2]:focus,arc_sf2[k2]:focus,arc_sf3[k2]:focus,arc_sf4[k2]:focus},
                var = {focus}, focus = 174.69941881
dip_sex:overlay={edge_dip:b2,midd_dip:b2}, var = {b2}!,b2 = -12.8161380375

!dip_mid:marker,superimpose,ref = midd_dip, offset = 0,ref_origin =center, ele_origin = center

fba_drifti:drift,L=drift_length/3
fba_drifto:drift,L=drift_length/2

tba_beg:marker
tba_end:marker

str2arc:marker

tba_arc:line=(str2arc,edge_fquad,fba_drifto,2*edge_dquad,fba_drifto,
                tba_beg,edge_dip,fba_drifti,mid_fquad,fba_drifti,mid_fquad,fba_drifti,
                midd_dip,fba_drifti,mid_fquad,fba_drifti,mid_fquad,fba_drifti,
                midd_dip,fba_drifti,mid_fquad,fba_drifti,mid_fquad,fba_drifti,
                midd_dip,fba_drifti,mid_fquad,fba_drifti,mid_fquad,fba_drifti,
                edge_dip,tba_end,fba_drifto,2*edge_dquad,fba_drifto,edge_fquad,
                str2arc)
tba_arc_closed:line=(2*tba_arc)
use,tba_arc
!-----
EDGE_FQUAD[K1] = 3.09273207594915E+00
MID_FQUAD[K1] = 1.24911958085089E+01
EDGE_DQUAD[K1] = -1.75424308161356E-03
EDGE_DIP[K1] = -3.22121444392064E+00
MIDD_DIP[K1] = -2.48408319508227E+00
!-----
! DIP_SEX[FOCUS] = -1.78885887599440E+01
! ARC_SEX[FOCUS] = 2.35968889193645E+02
!-----
cavity:rhcavity,l=0.8,voltage=450e3,harmon=10,superimpose,ref = 129, offset = 0,
                ref_origin = center, ele_origin = center
zero_point:fiducial, origin_ele = 133
!-----

!-----
!~match lines
!-----

!-----
!Straight Section
!-----

L_cell=1.1*cell_length

str_drift:drift,L=((L_cell/2)-2*quad_length-2*sex_length)
str_drift_chic:drift,L=((L_cell/2)-quad_length)
str_qf:quadrupole,L=quad_length/2,k1=edge_fquad[k1]
str_qd:quadrupole,L=quad_length/2
str_sf:sextupole,L=sex_length

```

```

str_sd:sextupole,L=sex_length

str_foc:marker
str_def:marker
chic_beg:marker
chic_end:marker

!str:line=(str_qf,str_sf,str_drift,str_qd,str_def,str_qd,str_sd,str_drift,str_qf,str_foc)
str:line=(EDGE_FQUAD,str_sf,str_drift,str_qd,str_def,str_qd,str_sd,str_drift,EDGE_FQUAD,str_foc)
use, str
!-----
EDGE_FQUAD[K1] = 3.06357595872161870E+000
MID_FQUAD[K1] = 1.25983648150456258E+001
EDGE_DQUAD[K1] = -9.40230260185378162E-003
STR_QD[K1] = -3.00106109855128445E+000
EDGE_DIP[K1] = -3.29212182468477943E+000
MIDD_DIP[K1] = -2.53523369616839434E+000
DIP_SEX[B2] = -2.24920670515815985E-003
ARC_SF1[K2] = 2.51685641178211199E+002
ARC_SF2[K2] = 1.97541452872327511E+002
ARC_SF3[K2] = 2.26908132981568599E+002
ARC_SF4[K2] = 2.89036261261280401E+002
STR_SF[K2] = 8.44737477223389561E+001
STR_SD[K2] = -8.47142676575588283E+000
!-----
ring:line=(tba_arc,3*str,tba_arc,3*str)

use,ring

*[aperture_type] = elliptical
*[aperture_at] = both_ends
*[x_limit] = 0.04/2
*[y_limit] = 0.04/2

sbend:.*[ds_step] = 5e-2
sbend:.*[r0_mag] = 30e-3/2

quadrupole:.*[ds_step] = 5e-2
quadrupole:.*[r0_mag] = 30e-3/2

sextupole:.*[ds_step] = 5e-2
sextupole:.*[r0_mag] = 30e-3/2

*[scale_multipoles] = T

```

B Coordinate Transformation *action-angle*

We can write a simplified version of the Hamiltonian,

$$H = \frac{p^2}{2} + \frac{K(s)}{2}x^2 \quad (52)$$

where we describe the reference particle only allowing only horizontal motion. We also describe transverse field ($A_x = A_y = 0$) only with no skew field. The periodic function $K(s)$, ($K(s) = \frac{1}{B\rho} \frac{\partial B_y}{\partial B_x}$) equals $K(s + C)$ where C is the circumference $2\pi R$. The momentum p , is in the normal plane and $p = \frac{dx}{ds}$. The common periodic solution of the Hamiltonian for the motion, x of the particle is:

$$x(s) = \sqrt{\epsilon_x \beta_x(s)} \cos(\phi(s) + \phi_0) \quad (53)$$

where we define the phase advance $\phi_x(s) = \int_0^s \frac{ds}{\beta_x(s)}$. If we switch to the action-angle variables, J and ψ , then the Hamiltonian can now be derived by:

$$\begin{aligned}\psi &= \int_0^s \frac{ds'}{\beta_x(s')} + \phi_0 \\ F_1(x, \psi, s) &= \frac{x^2}{2\beta} \left(\tan \psi - \frac{\beta'}{2} \right)\end{aligned}\tag{54}$$

where $F_1(x, \psi, s)$ is the generating function. We define $p = \frac{\partial F_1}{\partial x}$ and $J = \frac{\partial F_1}{\partial \psi}$. We can write a new Hamiltonian as,

$$\mathcal{H} = H + \frac{\partial F_1}{\partial s}\tag{55}$$

We have $p = x'$,

$$\begin{aligned}x' &= -\frac{x}{\beta} \left(\tan \psi - \frac{\beta'}{2} \right) \\ \tan^2 \psi &= \left[x' - \left(\frac{\beta' x}{2\beta} \right) \frac{\beta}{x} \right]^2 \\ J = \frac{\partial F_1}{\partial \psi} &= \frac{x^2}{2\beta} \sec^2 \psi = \frac{x^2}{2\beta} [1 + \tan^2 \psi] \\ &= \frac{x^2}{2\beta} \left[1 + \left(\left(x' - \frac{\beta' x}{2\beta} \right) \frac{\beta}{x} \right)^2 \right]^2\end{aligned}\tag{56}$$

The Courant and Snyder invariant, J , of the particle motion can be expressed as the emittance, ϵ , by

$$\epsilon = 2J = \frac{1}{\beta} \left[x^2 + \left(\beta x' - \frac{\beta' x}{2} \right)^2 \right]\tag{57}$$

The action of the particle is:

$$J = \frac{2}{\epsilon} = \frac{1}{2\beta} \left[x^2 + \left(\beta x' - \frac{\beta' x}{2} \right)^2 \right]\tag{58}$$

We have $\mathcal{H}(J, \psi) = \frac{J}{\beta(s)}$, where s is still an independent. From the Hamiltonian equations, $\frac{d\psi}{ds} = \frac{\partial \mathcal{H}}{\partial J} = \frac{1}{\beta(s)}$. Remember, $\int_0^s \frac{ds}{\beta_x(s)}$ is the phase advance and

$$\begin{aligned}x &= \sqrt{2\beta J} \cos \psi, \\ x' &= \sqrt{2\beta J} \left[\sin \psi - \frac{\beta'}{2} \cos \psi \right]\end{aligned}\tag{59}$$

We again rewrite the Hamiltonian,

$$\begin{aligned}F_2(\psi, J_1) &= J_1 \left[\frac{2\pi\nu s}{C} - \int_0^s \frac{ds'}{\beta_x(s')} \right] + \psi J_1 \\ \psi_1 = \frac{\partial F_2}{\partial J_1} &= \psi + \frac{2\pi\nu s}{C} - \int_0^s \frac{ds'}{\beta_x(s')}\end{aligned}\tag{60}$$

with $J_1 = \frac{\partial F_2}{\partial \psi} = J$ and

$$H_1 = \frac{2\pi\nu}{C} J_1\tag{61}$$

C Resonance Basis

Normal Forms are symplectic matrices that become “pure” rotations that have the dynamics of a given transfer matrix \mathcal{M} .

$$\mathcal{R} = A\mathcal{M}A^{-1} \quad (62)$$

where A is normalizing map \mathcal{M} . \mathcal{R} is the normal form of \mathcal{M} . The resonance basis can be generated by [40]:

$$\begin{aligned} f_2 &= \sum_{k=1}^N \frac{\phi_k}{2} [x_k^2 + (\mathcal{E}_k - \bar{\mathcal{E}}_k)p_k^2] = \sum_{k=1}^N f_2^k \\ \mathcal{R} &= e^{i f_2} \\ [f_2, h_k^\pm] &= \frac{\partial f_2}{\partial x} \frac{\partial h_k^\pm}{\partial p} - \frac{\partial f_2}{\partial p} \frac{\partial h_k^\pm}{\partial x} \\ &= \mp (i\mathcal{E}_k + \bar{\mathcal{E}}_k) \phi_k h_k^\pm = \mp \lambda h_k^\pm \\ h_k^\pm &= x_k \pm (i\mathcal{E}_k + \bar{\mathcal{E}}_k) p_k \\ &= \sqrt{2J_k} e^{\pm i\phi_k} = \sqrt{2J_k} \cos \phi_k \pm i\sqrt{2J_k} \sin \phi_k \end{aligned} \quad (63)$$

where x_k and p_k are the position and momentum variables for a given plane x , y , and z . For stable systems, $\mathcal{E}_n = 1$ and $\bar{\mathcal{E}}_n = 0$. The linear map generator, $h_2 = f_2$, is a *effective Hamiltonian* of the total Lie map where

$$M = A^{-1}TA \quad (64)$$

The T matrix is the linear transformation

$$T = \begin{pmatrix} T_{11} & T_{12} & 0 & 0 & 0 & \eta(s) - T_{11}\eta(0) - T_{12}\eta'(0) \\ T_{21} & T_{22} & 0 & 0 & 0 & \eta'(s) - T_{21}\eta(0) - T_{22}\eta'(0) \\ 0 & 0 & T_{33} & T_{34} & 0 & 0 \\ 0 & 0 & T_{43} & T_{44} & 0 & 0 \\ A & B & 0 & 0 & 1 & -C\alpha_c + A_\eta \sin \mu_x \\ 0 & 0 & 0 & 0 & 0 & 1 \end{pmatrix} \quad (65)$$

where α_c is the momentum compaction and $\mu(x)$ is the phase advance for the closed periodic lattice. The elements are defined as

$$\begin{aligned} T_{11} &= \cos \mu_x + \alpha_x \sin \mu_x \\ T_{12} &= \beta_x \sin \mu_x \\ T_{21} &= -\gamma_x \sin \mu_x \\ T_{22} &= \cos \mu_x - \alpha_x \sin \mu_x \\ T_{33} &= \cos \mu_y + \alpha_y \sin \mu_y \\ T_{34} &= \beta_y \sin \mu_y \\ T_{43} &= -\gamma_y \sin \mu_y \\ T_{44} &= \cos \mu_y - \alpha_y \sin \mu_y \\ A &= \eta' - \eta' T_{11} + \eta T_{21} \\ B &= -\eta - \eta T_{22} + \eta' T_{12} \end{aligned} \quad (66)$$

and $A_\eta = \gamma_x \eta^2 + 2\alpha_x \eta \eta' + \beta_x \eta'^2$. From here, the M matrix can be simplified as

$$M = \begin{pmatrix} \cos \mu_x & \sin \mu_x & 0 & 0 & 0 & 0 \\ -\sin \mu_x & \cos \mu_x & 0 & 0 & 0 & 0 \\ 0 & 0 & \cos \mu_y & \sin \mu_y & 0 & 0 \\ 0 & 0 & -\sin \mu_y & \cos \mu_y & 0 & 0 \\ 0 & 0 & 0 & 0 & 1 & -\oint ds \eta(s) / \rho(s) \alpha_c \\ 0 & 0 & 0 & 0 & 0 & 1 \end{pmatrix} \quad (67)$$

The *action-angle* transformation allow us to write h_s as

$$h_2 = -\mu_x J_x - \mu_y J_y - \frac{1}{2} \alpha_c \delta^2 \quad (68)$$

The eigenmodes of h_2 are

$$|ijkl, m \rangle = J_x^{(i+j)/2} J_y^{(k+l)/2} e^{(i-j)\phi_x} e^{(k-l)\phi_y} \delta^m \quad (69)$$

here we have that

$$: h_2 : |ijkl, m \rangle = \hat{i}[(i-j)\mu_x + (k-l)\mu_y] |ijkl, m \rangle \quad (70)$$

We have now that $|ijkl, m \rangle$ are the resonance basis. The eigenmode expansion of the *effective Hamiltonian* to the n^{th} generator can be written as:

$$h_n = \sum_{ijklm \geq 0} A_{ijklm}^n |ijkl, m \rangle \quad (71)$$

where $i + j + k + l + m = n$ the resonance order.

D Definition of Chirikov Criterion

Let us start with the definition of a integrable Hamiltonian with action J and constants α , β , and m ,

$$H_0 = \alpha J + \beta J^m \quad (72)$$

The Hamiltonian equations are

$$\begin{aligned} \frac{dJ}{dt} &= -\frac{\partial H_0}{\partial \phi} = 0 \\ \frac{d\phi}{dt} &= \alpha + \beta m J^{m-1} \equiv \omega(J) \end{aligned} \quad (73)$$

The solution are of $J = \text{invariant}$ and $\phi = \omega(J)t + \phi_0$. The perturbed Hamiltonian may be written as [41]:

$$H = H_0 + \epsilon H_\lambda = H_0 + \epsilon \cos \phi \sum_{l=-\infty}^{\infty} \delta(t-l) \quad (74)$$

where l is an integer and ϵ is the perturbation width or size. Let us rewrite $\sum_{l=-\infty}^{\infty} \delta(t-l)$ as $\lambda + 2 \sum_{m=\lambda}^{\infty} \cos 2\pi m t$. The perturbation period is defined as $\omega_0 = 2\pi$. The Hamiltonian can now be written as

$$H = \alpha J + \beta J^m + \frac{\epsilon \omega_0}{2\pi} \left(\cos(\phi) + \sum_{m=\lambda}^{\infty} (\cos(\phi + m\omega_0 t) + \cos(\phi - m\omega_0 t)) \right) \quad (75)$$

For small ϵ , we find $\cos \omega(J)t \pm m\omega_0 t$. When the function,

$$m\omega(J) = \pm m\omega_0 \quad (76)$$

a resonance is generated. The system is dominated by a single resonance if the action is at the resonance condition and the perturbation term is small. The Hamiltonian about the resonance is:

$$H_r = \alpha J + \beta J^m + \frac{\epsilon \omega_0}{2\pi} \cos(\phi - m\omega_0 t) \quad (77)$$

The Hamiltonian equations of motion are:

$$\begin{aligned} \frac{dJ}{dt} &= -\frac{\partial H_r}{\partial \phi} = \frac{\epsilon \omega_0}{2\pi} \sin(\phi - m\omega_0 t) \\ \frac{d\phi}{dt} &= \frac{\partial H_r}{\partial J} = \alpha + \beta m J^{m-1} = \omega(J) \end{aligned} \quad (78)$$

We have that the action, J , can be expressed as,

$$J = J_R + \delta J \quad (79)$$

and $\omega(J_R) = m\omega_0$. We can approximate the difference in the resonances as,

$$\begin{aligned} \frac{d(\phi - m\omega_0 t)}{dt} &= \omega(J) - \omega(J_R) \\ &= \omega(J) - m\omega_0 \\ &\simeq \Delta J \frac{d\omega(J_R)}{dJ} \equiv \Delta J \omega'(J_R) \end{aligned} \quad (80)$$

We let $\psi = \phi - m\omega_0 t$, and write the Hamiltonian equations of motion as

$$\begin{aligned} \frac{d\psi}{dt} &= \Delta J \omega'(J_R) \\ \frac{d\Delta J}{dt} &= \frac{\epsilon\omega_0}{2\pi} \sin \psi \end{aligned} \quad (81)$$

The resonance width can be described as

$$\delta J = 4 \sqrt{\left| \frac{\epsilon\omega_0}{2\pi\omega'(J_R)} \right|} \quad (82)$$

A plausible condition for the occurrence of the stochastic instability seems to be the approach of resonances down to the distance of the order of a resonance size [42]. The reason why the motion of the system is known as stochastic, is due to the unstable motion of the system as though a random force was applied.

From the distance between resonances, $\Delta\omega = \omega_0$, and the width of resonances, $\delta\omega \simeq \frac{d\omega}{dJ} \delta J = 4 \sqrt{\left| \frac{\epsilon\omega_0\omega'(J_R)}{2\pi} \right|}$, we can define the Chirikov Criterion

$$s = \frac{\delta\omega}{\Delta\omega} = 4 \sqrt{\left| \frac{\epsilon\omega'(J_R)}{2\pi\omega_0} \right|} \geq 1 \quad (83)$$

where we define s as the stochasticity parameter.

E W-function Derivation

If we allow $\delta = \frac{\Delta p}{p}$

$$\begin{aligned} \beta_\delta &= \beta(\delta), \alpha_\delta = \alpha(\delta), \phi_\delta = \phi(\delta) \\ \beta_0 &= \beta(0), \alpha_0 = \alpha(0), \phi_0 = \phi(0) \end{aligned} \quad (84)$$

where α and β are the Twiss parameters and ϕ the phase advance. We define the difference in the β function for the particle with momentum error, δp , and the particle on momentum, p , as $\Delta\beta$. Analogously, we define $\Delta\phi$ as the difference particle with momentum error and the on momentum particle.

$$\begin{aligned} \Delta\beta &= \beta_\delta - \beta_0, \beta = \sqrt{\beta_\delta\beta_0} \\ \Delta\phi &= \phi_\delta - \phi_0, \phi = \frac{\phi_\delta + \phi_0}{2} \end{aligned} \quad (85)$$

We can define the chromatic β -beat, B and chromatic change in the β function slope with respect to the position, A , in the magnetic lattice as [43]:

$$\begin{aligned} B &= \frac{\beta_\delta - \beta_0}{\sqrt{\beta_\delta\beta_0}} = \frac{\Delta\beta}{\beta} \\ A &= \frac{\alpha_\delta\beta_0 - \alpha_0\beta_\delta}{\sqrt{\beta_\delta\beta_0}} \end{aligned} \quad (86)$$

Through achromatic regions $A^2 + B^2$ is invariant, and if we both variables to δ we have:

$$\begin{aligned}
 B &= \lim_{\delta \rightarrow 0} \frac{\beta_\delta - \beta_0}{\sqrt{\beta_\delta \beta_0}} \times \frac{1}{\delta} \\
 A &= \lim_{\delta \rightarrow 0} \frac{\alpha_\delta \beta_0 - \alpha_0 \beta_\delta}{\sqrt{\beta_\delta \beta_0}} \times \frac{1}{\delta} \\
 W &= \sqrt{A^2 + B^2}
 \end{aligned} \tag{87}$$

F Damping Ring as RCS Booster

The RCS dipole field at injection is unstable due to the main field and multipole field becoming unpredictable at 6.3369×10^{-3} . To correct this issue, developing the damping ring to ramp to 1 GeV has been proposed. The dipole strength of the DR at 1 GeV is 3.13 T which enters the superconducting regime. A table of the key parameter changes with respect to energy are shown in Tab. 6.

Table 6: Key parameters of the Damping Ring with energies greater than 450 MeV.

Energy (MeV)	U_0 (KeV)	Damping Time (ms)	α_x (1/s)	α_y (1/s)	α_z (1/s)	ϵ_x nm	δ $\times 10^{-4}$
400	2.12	9.00	6.9×10^{-6}	2.7×10^{-6}	1.1×10^{-6}	41.52	7.25
500	5.19	4.61	1.3×10^{-5}	5.2×10^{-6}	2.2×10^{-6}	64.87	9.07
600	10.75	2.67	2.3×10^{-5}	9.0×10^{-6}	3.8×10^{-6}	93.41	10.88
700	19.92	1.68	3.7×10^{-5}	1.4×10^{-5}	6.0×10^{-6}	127.15	12.69
800	33.98	1.12	5.5×10^{-5}	2.1×10^{-5}	8.9×10^{-6}	166.07	14.50
900	54.43	0.79	7.8×10^{-5}	3.0×10^{-5}	1.3×10^{-5}	210.18	16.32
1000	82.96	0.58	1.1×10^{-4}	4.1×10^{-5}	1.7×10^{-5}	259.47	18.13

References

- [1] EIC collaboration, *Electron-Ion Collider at Brookhaven National Laboratory Conceptual Design Report*. Collider-Accelerator Department, Upton, NY, 17 ed., October 2020.
- [2] G. H. A. Febel, “Pia, the positive intensity accumulator for the petra injection,” *IEEE Transactions on Nuclear Science*, vol. NS-26, pp. 3244–3245, June 1979.
- [3] T. Faisst, “Untersuchungen am Positronenstrahl im Speicherring PIA am DESY,” Tech. Rep. 12, Deutsches Elektronen-Synchrotron, Bahrenfeld, Hamburg, Oktober 1981. DESY M-81/29.
- [4] M. Aiba, “Review of Top-Up Injection Schemes for Electron Storage Rings,” *9th International Particle Accelerator Conference*, pp. 1745–1750, 2018. Beam Dynamics and EM Fields.
- [5] D. Sagan, “Bmad: A relativistic charged particle simulation library,” *Nucl. Instrum. Meth.*, vol. A558, no. 1, pp. 356–359, 2006. Proceedings of the 8th International Computational Accelerator Physics Conference.
- [6] R. Chasman, G. K. Green, and E. M. Rowe, “Preliminary design of a dedicated synchrotron radiation facility,” *IEEE Transactions on Nuclear Science*, vol. 22, no. 3, pp. 1765–1767, 1975.
- [7] A. Wolski, “Lattice Design for an ILC Damping Ring with 3 km Circumference,” Tech. Rep. LBNL-56506, Lawrence Berkeley National Laboratory, Berkeley, CA, October 2004. <http://repositories.cdlib.org/lbnl/LBNL-56506>.
- [8] G. R. White, Y. Cai, R. Hettel, M. Johansson, V. Yakimenko, G. Yocky, “A Compact 335 MeV Positron Damping Ring Design for FACET-II,” *Proceedings of IPAC2017*, pp. 3652–3655, 2017. Beam Dynamics and EM Fields.
- [9] CERN, *CAS - CERN Accelerator School : Accelerator Physics, Oxford, UK 16 - 27 Sep 1985. CAS - CERN Accelerator School : Accelerator Physics*, (Geneva), CERN, 1987.
- [10] CERN, *CAS - CERN Accelerator School : 5th Advanced Accelerator Physics Course: Rhodes, Greece 20 Sep - 1 Oct 1993. CAS - CERN Accelerator School : 5th Advanced Accelerator Physics Course*, (Geneva), CERN, 1995.
- [11] J. Gao, “Analytical estimation of the dynamic apertures of circular accelerators,” *Nuclear Instruments and Methods in Physics Research Section A: Accelerators, Spectrometers, Detectors and Associated Equipment*, vol. 451, pp. 545–557, 05 2000.
- [12] R. H. Helm, M. J. Lee, P. L. Morton, and M. Sands, “Evaluation of synchrotron radiation integrals,” *IEEE Trans. Nucl. Sci.*, vol. 20, pp. 900–901, 1973.
- [13] J. M. Jowett, “Introductory statistical mechanics for electron storage rings,” *AIP Conference Proceedings*, vol. 153, pp. 864–970, 02 1987.
- [14] R. Q. Twiss and N. H. Frank, “Orbital Stability in a Proton Synchrotron,” *Review of Scientific Instruments*, vol. 20, pp. 1–17, 12 1949.
- [15] E. D. Courant, M. S. Livingston, and H. S. Snyder, “The strong-focusing synchrotron—a new high energy accelerator,” *Phys. Rev.*, vol. 88, pp. 1190–1196, Dec 1952.
- [16] E. Courant and H. Snyder, “Theory of the alternating-gradient synchrotron,” *Annals of Physics*, vol. 3, no. 1, pp. 1–48, 1958.
- [17] R.M. Bergmann, T. Bieri, P. Craievich, Y. Ekinici, T. Garvey, C. Gough, M. Negrazus, L. Rivkin, C. Rosenberg, L. Schulz, T. Schmidt, L. Stingelin, A. Streun, V. Vrankovic. A. Wrulich, A. Zandonella Callegher, R. Zennaro, “A COMPACT STORAGE RING FOR THE PRODUCTION OF EUV RADIATION,” *ANS AccApp '17 Thirteenth International Topical Meeting on the Applications of Accelerators*, 2017. <http://accapp17.org/wp-content/uploads/2017/09/AppAcc-paper.pdf>.

- [18] A. Dragt and C. P. C. f. T. P. University of Maryland, *Lie Methods for Nonlinear Dynamics with Applications to Accelerator Physics*. University of Maryland, Center for Theoretical Physics, Department of Physics, 1997.
- [19] A. Deprit, “Canonical transformations depending on a small parameter,” *Celestial mechanics*, vol. 1, pp. 12–30, Mar 1969.
- [20] E. D. Courant, “Parameterization of transport and period matrices with x-y coupling,” tech. rep., Brookhaven National Laboratory, 7 1990.
- [21] M. Giovannozzi and E. Todesco, “Combined-function optics for circular high-energy hadron colliders,” *The European Physical Journal Plus*, vol. 137, p. 361, Mar 2022.
- [22] M. Titze, “Approach to combined-function magnets via symplectic slicing,” *Phys. Rev. Accel. Beams*, vol. 19, p. 054002, May 2016.
- [23] V. Ziemann and A. Streun, “Equilibrium parameters in coupled storage ring lattices and practical applications,” *Phys. Rev. Accel. Beams*, vol. 25, p. 050703, May 2022.
- [24] N. e. a. Tsoupas, “The erhic spin rotator and the beam optics of the 400 mev transfer line to rcs,” *International Journal of Modern Physics A*, vol. 34, 12 2019.
- [25] M. Aiba, M. Böge, F. Marcellini, A. Saá Hernández, and A. Streun, “Longitudinal injection scheme using short pulse kicker for small aperture electron storage rings,” *Phys. Rev. ST Accel. Beams*, vol. 18, p. 020701, Feb 2015.
- [26] M. Aiba, B. Goddard, K. Oide, Y. Papaphilippou, . Sa Hernandez, D. Shwartz, S. White, and F. Zimmermann, “Top-up injection schemes for future circular lepton collider,” *Nuclear Instruments and Methods in Physics Research Section A: Accelerators, Spectrometers, Detectors and Associated Equipment*, vol. 880, pp. 98–106, 2018.
- [27] S. Y. Lee, *Accelerator Physics*. WORLD SCIENTIFIC, 3rd ed., 2011.
- [28] D. T. Abell, “Numerical computation of high-order transfer maps for rf cavities,” *Phys. Rev. ST Accel. Beams*, vol. 9, p. 052001, May 2006.
- [29] T. Suzuki, “Synchrobetatron resonance driven by dispersion in rf cavities,” *Part. Accel.*, vol. 18, no. KEK-Preprint-84-21, pp. 115–128, 1985.
- [30] C. Corsten and H. Hagedoorn, “Simultaneous treatment of betatron and synchrotron motions in circular accelerators,” *Nuclear Instruments and Methods in Physics Research*, vol. 212, no. 1, pp. 37–46, 1983.
- [31] S. Y. Lee, “Single particle dynamics at synchro-betatron coupling resonances,” *Phys. Rev. E*, vol. 49, pp. 5706–5716, Jun 1994.
- [32] S. G. Peggs and R. M. Talman, “Nonlinear problems in accelerator physics,” *Annual Review of Nuclear and Particle Science*, vol. 36, no. 1, pp. 287–325, 1986.
- [33] D. R. Douglas, “Dynamic aperture calculations for circular accelerators and storage rings,” *AIP Conference Proceedings*, vol. 153, no. 1, pp. 390–473, 1987.
- [34] H. Goldstein, *Classical Mechanics*. Addison-Wesley, 1980.
- [35] J. Bengtsson, “The Sextupole Scheme for the Swiss Light Source (SLS): An Analytic Approach,” Tech. Rep. 9, Paul Scherrer Institut (PSI), Villeggen, Switzerland, March 1997.
- [36] Y. Luo, M. Bai, R. Calaga, J. Bengtsson, W. Fischer, N. Malitsky, F. Pilat, and T. Satogata, “Measurement and correction of third resonance driving term in the rhic,” in *2007 IEEE Particle Accelerator Conference (PAC)*, pp. 4351–4353, 2007.
- [37] C.-X. Wang, “Explicit formulas for 2nd-order driving terms due to sextupoles and chromatic effects of quadrupoles,” 4 2012.

- [38] K. P. Wootton, M. J. Boland, and R. P. Rassool, “Measurement of ultralow vertical emittance using a calibrated vertical undulator,” *Phys. Rev. ST Accel. Beams*, vol. 17, p. 112802, Nov 2014.
- [39] J. D. Bjorken and S. K. Mtingwa, “Intrabeam scattering,” *Part. Accel.*, vol. 13, no. FERMILAB-PUB-82-47-THY, pp. 115–143, 1982.
- [40] E. Forest, M. Berz, and J. Irwin, “Normal form methods for complicated periodic systems: a complete solution using differential algebra and lie operators,” *Part. Accel.*, vol. 24, pp. 91–107, 1989.
- [41] P. J. Channell, “An illustrative example of the chirikov criterion for stochastic instability,” *AIP Conference Proceedings*, vol. 46, no. 1, pp. 248–259, 1978.
- [42] B. V. Chirikov, “A universal instability of many-dimensional oscillator systems,” *Physics Reports*, vol. 52, no. 5, pp. 263–379, 1979.
- [43] B. W. S. L. Montague, “Chromatic effects and their first-order correction,” *CAS - CERN Accelerator School : Accelerator Physics*, 1987.